Chapter 4
Nanoscale First-Principles Electronic Structure Simulations of Materials Relevant to Organic Electronics

Susumu Yanagisawa and Ikutaro Hamada

Abstract Organic molecular materials have attracted considerable attention as a candidate for next-generation flexible electronics in the near future. However, there still remain open questions on fundamental electronic properties such as mechanisms of the carrier transport and barriers for carrier injection at organic-inorganic heterojunctions. In this review, we illustrate the progresses in first-principles electronic structure calculations of the materials for investigation of the atomic- or molecular-scale electronic properties of organic semiconductor materials, which are in general difficult to observe even with present-day experimental techniques. The theoretical studies not only help elucidate the mechanism of the experimental measurement but also may allow us to gain insights into the essences of the materials properties in terms of the electronic structure. Specifically, in this article, we focus on the first-principles theoretical treatment of the geometric configurations of organic semiconductors and their electronic structure at the level beyond the approximation to the density functional theory (DFT) such as the local density (LDA) and generalized gradient approximations (GGA), i.e., the van der Waals-inclusive methods for describing the weak intermolecular interaction in organic solids and the many-body perturbation theory within the GW approximation for treatment of the charged excitation (quasiparticle) and thus the fundamental gap and the band dispersion of the crystals. Here, we illustrate the recent studies on (i) the effect of the molecular configuration on the quasiparticle energy in organic semiconductors, (ii) the energy level alignment at organic-metal interfaces, and (iii) prediction of the charge injection levels at a surface of organic thin film, i.e., the ionization energy and the electron affinity. Further progresses in theoretical

S. Yanagisawa (✉)
Faculty of Science, Department of Physics and Earth Sciences, University of the Ryukyus, Nishihara, Okinawa, Japan
e-mail: shou@sci.u-ryukyu.ac.jp

I. Hamada
Department of Precision Science and Technology, Graduate School of Engineering, Osaka University, Suita, Osaka, Japan
e-mail: ihamada@prec.eng.osaka-u.ac.jp

T. Onishi (ed.), *Theoretical Chemistry for Advanced Nanomaterials*,
https://doi.org/10.1007/978-981-15-0006-0_4

methodologies, being enhanced by rapid progress in computational resource and algorithm, might lead to in silico material simulation or design.

Keywords Organic semiconductors · Intermolecular van der Waals interaction · van der Waals density functional · GW approximation · Organic-metal interfaces · Image potential states

4.1 Introduction

Semiconductors comprised of organic molecules have attracted considerable attention as candidates for next-generation flexible electronics materials. It is believed that organic semiconductor electronics will be competitive against inorganic semiconductors for applications to mechanically flexible, large-area, and low-cost electronics [1]. Some organic-based electronic devices such as organic light-emitting diodes (OLED) are on the market, while other electronics materials such as organic field-effect transistors (OFET) and organic photovoltaics (OPV) are at the stage of a fundamental research. However, there is much room for investigation on the electronic properties of the organic materials, for instance, carrier transport property. Poor knowledge of the transport property in organic solids is contrast to the situation in inorganic semiconductors [2]. More understanding of their basic electronic properties is urgent, which may accelerate development of the next-generation flexible electronics.

Here, we review recent theoretical works with the first-principles electronic structure calculation, i.e., (i) those on the intermolecular van der Waals (vdW) interaction dominating the structural and electronic properties of the organic semiconductor materials and (ii) the effect of the many-body electrons (or the quasiparticle effect) upon the injected charge in the bulk of the organic semiconductors or at the organic-metal interface.

We demonstrate the roles of the first-principles electronic structure calculations which could clarify a relation between the electronic structure and the geometrical configurations. As an example, the impact of the atomic-scale geometric structures on the electronic states is discussed. It was not possible to predict the crystal geometry or the molecular configuration in the unit cell of the organic semiconductor crystals with the density functional theory (DFT) within the local density (LDA) or generalized gradient approximation (GGA), because of the failure of the methodology to describe the intermolecular vdW interaction, which is nonlocal and long-ranged in nature. However, there are more and more methodologies being developed capable of describing the vdW interaction between the constituent organic molecules [3–11].

The quasiparticle energy is essentially related to the barrier for charge injection, i.e., the electronic energy upon charged excitation, and also the interaction between the electron-hole pair upon optical excitation, dominating the optical gap. Fundamental gap and band dispersion of organic molecular solids are becoming accurately

predictable by the first-principles theoretical methods describing the quasiparticle self-energy such as the GW approximation [12].

In this article, we review first-principles electronic structure calculations on

1. Structures of organic semiconductor crystals with the van der Waals (vdW)-inclusive methods
2. Electronic properties of organic-metal interfaces: electronic properties such as energy level alignment and the image potential states
3. Electronic charge (electron or hole) injection level depending on the molecular orientation at the organic crystal surface

In the first topic, we focus on our first-principles study on prediction of the lattice constants and the intermolecular configuration in oligoacene crystals, along with analysis of the band structure and the intermolecular transfer integral [13]. Here, the Wannier functions [14, 15] were derived, allowing us to estimate intermolecular transfer integrals depending crucially on the cell volume or the intermolecular configurations in the crystal. The Wannier functions in organic crystals could be mapped on the crystal Hamiltonian such as the tight-binding Hamiltonian, thus leading to multi-scale real-time simulations of charge carrier transport in organic crystals [16]. In addition to the previous work on naphthalene, anthracene, and tetracene [13], calculation of pentacene and hexacene crystals is demonstrated in this article.

Secondly, the electronic properties induced at the organic-metal interface are discussed. The energy level alignment at the organic-metal interface originating from the rearrangement of the electronic clouds at the interface has attracted considerable attention [17], because of its relevance to barrier for charge injection into an organic layer. To elucidate the experimental measurements using techniques such as photoemission spectroscopy proving the energy levels of the injected hole or electron right at the interface, aid of a reliable theoretical method treating charged excitations (quasiparticles) is necessary. Here, we focus on highly accurate theoretical approaches beyond DFT within the LDA or GGA, such as the many-body perturbation theory within the GW approximation [12, 18]. In addition, we demonstrate our recent theoretical investigation [19] to clarify the electronic nature of the recently reported image potential state of graphite in the presence of an organic overlayer [20].

In the third place, we discuss determination of charge injection levels in organic semiconductor crystals or thin films, mainly based on the GW approximation. The charge injection level relative to the vacuum level, i.e., ionization energy (IE) or electron affinity (EA) of organic semiconductors, crucially affects the charged carrier transport properties. It was practically difficult to predict IE and EA of organic semiconductors using periodic slab models at the GW level of theory, because of the computational cost to meet convergence criteria. Recently, there are theoretical studies at the same level of theory handling the problem [21–23].

Finally, we demonstrate the future aspects of the theoretical methods, both in terms of contribution to elucidation of the novel experimental measurements and room for development of the theoretical methodologies.

4.2 Theoretical Investigations on Electronic Properties of Organic Molecular Materials

4.2.1 Structural Properties: Crystal Geometry and Intermolecular Configuration

4.2.1.1 Crystal Structures Optimized with a Variant of Van der Waal Density Functionals

Geometrical configurations in bulk systems of organic molecular crystals or heterojunctions such as organic-metal electrode and organic-organic interfaces are of importance, in which the atomistic- or molecular-scale geometrical arrangements significantly alter the electronic properties.

The structural properties of organic crystals such as crystal structures and intermolecular geometrical configurations are one of the central issues dominating the electronic properties such as charge transport [24, 25]. Subtle interplay among the intermolecular van der Waals (vdW) forces, the exchange repulsion, and the orbital hybridization leads to a rich variety of polymorphs with different electronic properties. The stability of the polymorphs depends on temperature, and thus attempts are going on to predict (meta-)stable polymorphs of the organic crystals [26]. Nevertheless, first-principles theoretical investigations on electronic structure of the most stable polymorph at 0 K may give us insights into the properties of the materials at not only low temperature but also at room temperature.

Recently proposed vdW-inclusive methods have played roles in prediction of stable crystal structure and molecular configurations, which allows us to discuss the effects of the intermolecular interaction on electronic properties.

Here, we focus on the first-principles theoretical methods that have been successfully applied to organic semiconductor crystals (for a variety of the applications to other molecular aggregates and complexes, see a recent comprehensive review such as Ref. [27]).

The structure and the energetics of an organic crystal could be quite accurately predicted with first-principles methods such as the adiabatic-connection fluctuation-dissipation theorem within the random-phase approximation (RPA) [4, 28, 29], the quantum Monte Carlo [30, 31], and the wave function-based quantum chemistry [32, 33] methods. However, the computational cost involved at present prevents application of the highly accurate methods to organic crystals that are of practical or experimental interest. The vdW-inclusive density functional method, such as the van der Waals density functional (vdW-DF) and its variants [10, 34–39], may be a method of choice, because of its moderate computational cost [40] and its reliability in prediction of structural properties of organic crystals. We employed the revised vdW-DF2 (rev-vdW-DF2), with its reliable prediction of crystal geometries of organic crystals such as rubrene [10] and metal phthalocyanine [41].

We first performed the structural optimizations and determined the stable structures for naphthalene, anthracene, and tetracene crystals (Fig. 4.1) by using

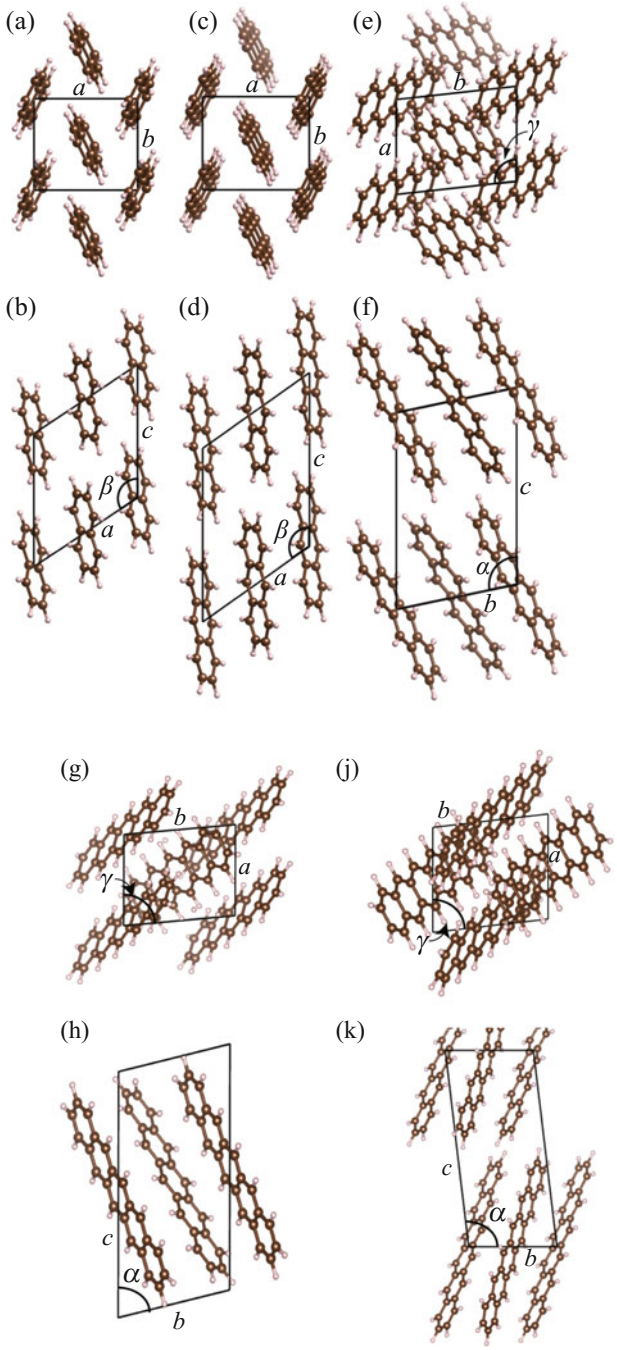

Fig. 4.1 Crystal structures of the single crystals of (**a**), (**b**): naphthalene, (**c**), (**d**): anthracene, (**e**), (**f**): tetracene, (**g**), (**h**): pentacene, and (**j**), (**k**): hexacene [42]. The unit cell consists of the two nonequivalent molecules placed at the corner and center of the cell, which are arranged in a herringbone fashion. For tetracene, the Niggli cell parameters are displayed, for ease of comparison between the crystal geometry obtained in this study and the experimental data (see Table 4.1). (Figure 1(**a**)–(**f**): Reprinted from [13], with the permission of AIP Publishing)

vdW-DF. As the initial structures for the structural optimization, we used the X-ray diffraction data of naphthalene [43] and anthracene [44] with the space group of $P2_1/a$ measured at 295 K and those of tetracene with the $P1$ symmetry reported by Robertson [45, 46]. For additional calculations in this work, we used the X-ray diffraction data of the pentacene crystalline phase obtained by vapor deposition [47]. The crystalline phase has spacing for the ac planes [(001)d spacing] of 1.45 nm [47], and similar spacing has been reported in other experiments of the single crystals [48–50]. Recent theoretical studies [51, 52] showed that with the recent vdW-inclusive method, similar polymorph is more stable than the other experimentally reported polymorphs such as the bulk phase reported by Campbell et al. [53] and the thin film phases [54, 55]. The initial crystal structure of hexacene came from the diffraction data at 123 K of the crystalline phase fabricated with physical vapor transport method [56]. For the total energy calculation, we used the projector augmented-wave (PAW) method [57] as implemented in the Vienna ab initio simulation package (VASP) [58, 59]. The vdW-DF calculations were performed using the Román-Pérez-Soler algorithm [40] implemented by Klimeš et al. [39]. We used the revised vdW-DF2 (rev-vdW-DF2) [10], which uses the revised Becke's exchange functional [60] and the nonlocal correlation for the second version of vdW-DF [37].

We used the kinetic energy cutoff of 1000 eV to expand the wave functions in terms of a plane-wave basis set, along with hardest PAW potentials supplied with the VASP code [61]. The Brillouin zone integration was performed using a $4 \times 4 \times 4$ Monkhorst-Pack (MP) [62] **k**-point set for naphthalene and anthracene, a $4 \times 4 \times 2$ MP **k**-point set for tetracene. In the calculations of pentacene and hexacene in this work, we used a $4 \times 3 \times 2$ and $4 \times 4 \times 2$ **k**-point set, respectively. Cell parameters and internal degrees of freedom were optimized until the forces acting on atoms became smaller than the threshold value of 1.0×10^{-3} eV Å^{-1}. With this setting the cell parameters and lattice energy are estimated to converge within 0.039 Å, 0.49°, and 2.37 Å^3 and 1 meV, respectively. The lattice energy was calculated by subtracting the sum of the total energies of the constituent molecules from that of the molecular crystal.

We also investigated the effect of the zero-point vibrational energy (ZPE) to the equilibrium volume for selected crystals as follows. Starting from the equilibrium crystal structure, the cell volume was varied by ±2% up to ±10%, and at each volume, we performed the fixed volume structural optimization followed by the normal mode analysis at the Γ point to calculate the ZPE contribution to the total energy. We then calculated the total energy with ZPE and fitted it to the Murnaghan [63] equation of state to get the ZPE corrected equilibrium volume.

Table 4.1 displays the resulting lattice constants. Overall, the cell parameters and equilibrium volumes are in reasonable agreement with experimental values in the literature, which were measured at 5−296 K [47, 48, 50, 56, 66, 67]. They are also comparable to other vdW-inclusive methods such as vdW-DF-cx [35],

more elaborated ones such as Tkatchenko-Scheffler vdW correction (TS-vdW) [5], that with the many-body dispersion (MBD) [8], and the exchange-hole dipole moment model with B86b exchange (B86b-XDM) [69, 70]. As for comparison to experiments, the average absolute relative deviations from the experimental values [50, 66, 67] are 0.6% (length) and 0.7% (angle) for naphthalene, 0.5% (length) and 0.02% (angle) for anthracene, and 1.0% (length) and 0.3% (angle) for tetracene. Among the three oligoacene crystals, the maximum absolute relative deviation of the lattice constants of 1.93% was found for b of tetracene crystal, the experimental value of which was measured at 175 K [50].

For pentacene, the absolute relative error from the experimental value measured at 295.5 K [47] is 1.5% (length) and 0.9% (angle) on average, and the maximum absolute relative deviation from experiments is found for b (2.98%). However, if the calculated values are compared to the measurement of the same polymorph at 90 K [48], the maximum absolute relative deviation decreases to 1.07% (b), and the average absolute relative deviations are 0.6% and 0.5% for the cell length and cell angle, respectively. The calculated lattice constants and equilibrium volume are also in good agreement with those predicted with vdW-DF-cx for the same polymorph [52]. In the case of hexacene, the absolute relative deviation from experiments is found to be largest of all the oligoacene crystals, i.e., the averaged deviation of 3.8% and 1.0% for length and angle, respectively, and the maximum deviation of 6.15% is found for length b, in comparison to the experimental values measured at 123 K [56]. The deviation might be diminished if the theoretical result was compared to experiments measured at lower temperature, as demonstrated for pentacene. In addition to that, one should take into account the thermal expansion of the volume at finite temperature, i.e., the vibrational effect of the crystal.

The effect of ZPE to the equilibrium volume was investigated by the fixed volume structural optimization, followed by the normal mode analysis at the Γ point. The ZPE effect was taken into account, while the volume was incrementally varied. The resulting volume of naphthalene and anthracene was reasonably larger than that determined without including ZPE (see Table 4.1). Here, the phonon frequency was calculated by sampling only the Γ-point. The deviation from experiments might decrease if the phonon frequencies in the entire Brillouin zone were taken into account.

The theoretical lattice energies per molecule of the oligoacene crystals, slightly underestimated, are in reasonable agreement with experiments, with the absolute relative deviations (deviations) being 5.2% (0.044 eV) and 8.6% (0.087 eV) for naphthalene and anthracene, respectively. Notice that they are in good agreement with those at the level of RPA with single excitations [29]. Taking into account the calculated lattice energy of the tetracene crystal (-1.383 eV), along with the theoretical vibrational contribution to the sublimation enthalpy of organic crystals ($0.07-0.11$ eV) [64], we estimate the theoretical sublimation enthalpy would be in agreement with the experimental value (-1.409 eV) [68] within 0.14 eV.

Table 4.1 Optimized lattice parameters (a, b, c, α, β, and γ), equilibrium volume (V_0), and lattice energies per molecule (E_b) of the naphthalene and anthracene crystals in the $P2_1/a$ symmetry, tetracene in the $P1$ symmetry, and pentacene single crystal in the $P\bar{1}$ symmetry obtained with rev-vdW-DF2, along with experimental values. The Niggli cell parameters are used for tetracene. (Reprinted from [13], with the permission of AIP Publishing)

	Naphthalene							
	a	b	c	α	β	γ	V_0	E_b
	(Å)	(Å)	(Å)	(deg)	(deg)	(deg)	(Å^3)	(eV)
rev-vdW-DF2[1]	8.012	5.898	8.609	90.00	124.12	90.00	336.8	−0.803
rev-vdW-DF2 (ZPE)[2]	—	—	—	—	—	—	347.2	—
PBE+TS-vdW[3]	8.109	5.884	8.660	90.00	124.05	90.00	342.32	−1.035
PBE+MBD[3]	7.970	5.868	8.570	90.00	123.11	90.00	335.70	−0.905
PBE0+MBD[3]	—	—	—	—	—	—	—	−0.885
B86b-XDM[4]	8.134	5.938	8.699	90.00	124.35	90.00	346.89	−0.784
B86b-XDM[5]	—	—	—	—	—	—	335.8	−0.790
vdW-DF-cx[6]	8.06	5.91	8.75	90.00	124.4	90.00	344.4	−0.92
Expt.	8.080[7]	5.933[7]	8.632[7]	90.00	124.65[7]	90.00	340.4[7]	−0.847[8]
	Anthracene							
	a	b	c	α	β	γ	V_0	E_b
	(Å)	(Å)	(Å)	(deg)	(deg)	(deg)	(Å^3)	(eV)
rev-vdW-DF2[1]	8.339	5.948	11.087	90.00	125.37	90.00	448.40	−1.081
rev-vdW-DF2 (ZPE)[2]	—	—	—	—	—	—	460.8	—
PBE+TS-vdW[3]	8.399	5.943	11.120	90.00	125.21	90.00	453.5	−1.392
PBE+MBD[3]	—	—	—	—	—	—	—	−1.262
PBE0+MBD[3]	—	—	—	—	—	—	—	−1.234
B86b-XDM[4]	8.452	5.985	11.168	90.00	125.43	90.00	460.32	−1.049
B86b-XDM[5]	—	—	—	—	—	—	448.4	−1.054
vdW-DF-cx[6]	8.38	5.96	11.23	90.00	125.6	90.00	456.5	−1.23
Expt.	8.37[9]	6.00[9]	11.12[9]	90.00	125.4[9]	90.00	455.205[9]	−1.168[8]

	Tetracene							
	a	b	c	α	β	γ	V_0	E_b
	(Å)	(Å)	(Å)	(deg)	(deg)	(deg)	(Å^3)	(eV)
rev-vdW-DF2[1]	6.019	7.686	12.489	100.83	99.62	94.36	556.00	−1.383
vdW-DF-cx[6]	6.05	7.69	12.53	100.2	100.1	94.5	561.3	−1.56
PBE+TS-vdW[6]	6.05	7.71	12.53	100.7	99.2	94.3	564.1	—
Expt.	6.0565[10]	7.8376[10]	12.5523[10]	101.2749[10]	99.4529[10]	94.2080[10]	572.968[10]	−1.409[11]
	Pentacene							
	a	b	c	α	β	γ	V_0	E_b
	(Å)	(Å)	(Å)	(deg)	(deg)	(deg)	(Å^3)	(eV)
rev-vdW-DF2[1]	6.268	7.554	14.297	77.51	88.46	84.21	657.56	−1.70
vdW-DF-cx[6]	6.29	7.52	14.35	77.8	88.7	84.1	660.3	−1.92
Expt.[12]	6.265	7.786	14.511	76.65	87.50	84.61	685.49	—
Expt.[13]	6.239	7.636	14.330	76.978	88.136	84.415	661.94	—

(continued)

Table 4.1 (continued)

	Hexacene							
	a	b	c	α	β	γ	V_0	E_b
	(Å)	(Å)	(Å)	(deg)	(deg)	(deg)	(Å^3)	(eV)
rev-vdW-DF2[1]	6.512	7.223	16.140	96.60	91.42	96.42	748.91	−2.02
vdW-DF-cx[6]	6.61	7.05	16.14	95.8	91.5	96.8	743.3	−2.30
Expt.[14]	6.306	7.697	16.480	98.77	91.25	95.81	785.92	—

[1]This work. ZPE is not taken into account
[2]This work. ZPE is included
[3]Ref. [64]
[4]Ref. [7] Lattice energy with ZPE
[5]Ref. [65]
[6]Ref. [52]
[7]Ref. [66] (5 K)
[8]Ref. [64] Experimental sublimation enthalpy with the theoretical ZPE subtracted.
[9]Ref. [67] (16 K)
[10]Ref. [50] (175 K)
[11]Ref. [68] Experimental sublimation enthalpy
[12]Ref. [47] (295.5 K)
[13]Ref. [48] (90 K)
[14]Ref. [56] (123 K)

4.2.1.2 Electronic Structures with the *GW* Approximation

To confirm reliability of the theoretical crystal geometries of the oligoacenes predicted with the vdW-DF method, we investigated the electronic structures for the optimized crystal geometries using the many-body perturbation theory within the *GW* approximation [13]. Here, we considered naphthalene, anthracene, tetracene, and pentacene crystals, of which the experimental fundamental gap or the density of states (DOS) were reported [71–81].

The quasiparticle energy in solids within the *GW* approximation is calculated with [18]

$$E_{n\mathbf{k}}^{\mathrm{qp}} = \epsilon_{n\mathbf{k}}^{\mathrm{DFT}} - \langle \phi_{n\mathbf{k}}^{\mathrm{DFT}} | V_{xc}^{\mathrm{DFT}} | \phi_{n\mathbf{k}}^{\mathrm{DFT}} \rangle + \langle \phi_{n\mathbf{k}}^{\mathrm{DFT}} | \Sigma(E_{n\mathbf{k}}^{\mathrm{qp}}) | \phi_{n\mathbf{k}}^{\mathrm{DFT}} \rangle \,, \tag{4.1}$$

where $\epsilon_{n\mathbf{k}}^{\mathrm{DFT}}$ and $\phi_{n\mathbf{k}}^{\mathrm{DFT}}$ are starting eigenvalues and wave functions, respectively (in general DFT-LDA or DFT-GGA), i.e., a starting mean-field approximation which is to be perturbed by the many-body effect. $\mathrm{V}_{xc}^{\mathrm{DFT}}$ is the corresponding exchange-correlation potential of the mean field, and the self-energy operator $\Sigma(E_{n\mathbf{k}}^{\mathrm{qp}})$ describes all the ingredients of the many-body effect. The self-energy operator, formally obtained as expansion of the self-energy in the Hedin equation to first-order in the screened Coulomb potential W [12], results in formulations computed on numerical grids. For instance, in the *GW* space-time formalism, the self-energy operator is calculated in real space ($\mathbf{r}, \mathbf{r}\prime$) and imaginary time ($i\tau$) [82–84],

$$\Sigma(\mathbf{r}, \mathbf{r}'; i\tau) = iG(\mathbf{r}, \mathbf{r}'; i\tau)W(\mathbf{r}, \mathbf{r}'; i\tau), \tag{4.2}$$

and its diagonal matrix elements are computed, followed by the analytic continuation of the matrix elements to the real frequency axis [82, 83]. G $(\mathbf{r}, \mathbf{r}'; i\tau)$ is the noninteracting Green's function in real space and in imaginary time for propagation of the hole ($\tau > 0$) and the electron ($\tau < 0$), respectively,

$$G(\mathbf{r}, \mathbf{r}'; i\tau) = \begin{cases} i\Sigma_{n\mathbf{k}}^{occ} \phi_{n\mathbf{k}}(\mathbf{r}) \phi_{n\mathbf{k}}^*(\mathbf{r}') \exp(\epsilon_{n\mathbf{k}}\tau) & (\tau > 0), \\ -i\Sigma_{n\mathbf{k}}^{unocc} \phi_{n\mathbf{k}}(\mathbf{r}) \phi_{n\mathbf{k}}^*(\mathbf{r}') \exp(\epsilon_{n\mathbf{k}}\tau) & (\tau < 0), \end{cases} \tag{4.3}$$

constructed from the Kohn-Sham eigenfunctions and eigenvalues, and $\mathbf{k}$ vectors denote those in the first Brillouin zone. The irreducible polarization P within the random-phase approximation is calculated in real space and imaginary time,

$$P(\mathbf{r}, \mathbf{r}'; i\tau) = -2iG(\mathbf{r}, \mathbf{r}'; i\tau)G(\mathbf{r}', \mathbf{r}; -i\tau), \tag{4.4}$$

which is Fourier transformed to $P_{\mathbf{GG}'}(\mathbf{k}; i\omega)$ in reciprocal space. The symmetrized dielectric matrix in reciprocal space $\tilde{\epsilon}_{\mathbf{GG}'}(\mathbf{k}; i\omega)$ is constructed as

$$\tilde{\epsilon}_{\mathbf{GG}'}(\mathbf{k}; i\omega) = \delta_{\mathbf{GG}'} - \frac{4\pi}{|\mathbf{k}+\mathbf{G}||\mathbf{k}+\mathbf{G}'|} P_{\mathbf{GG}'}(\mathbf{k}; i\omega). \tag{4.5}$$

Then, $W(\mathbf{r}, \mathbf{r}'; i\tau)$ is obtained by Fourier transforming to real space and imaginary time the screened Coulomb potential in reciprocal space and imaginary frequency,

$$W_{\mathbf{GG}'}(\mathbf{k}; i\omega) = \frac{4\pi}{|\mathbf{k}+\mathbf{G}||\mathbf{k}+\mathbf{G}'|} \tilde{\epsilon}^{-1}_{\mathbf{GG}'}(\mathbf{k}; i\omega). \tag{4.6}$$

The quantities defined in Eqs. 4.1, 4.2, 4.3, and 4.6 are, practically, calculated only once with the starting eigenvalues and wave functions, i.e., one-shot G_0W_0 calculations.

We performed the electronic structure calculations using the modified version of the GW space-time code [82–84], which enables highly parallelized calculations with thousands of CPU cores. Our perturbative G_0W_0 calculations were based on the norm-conserving pseudopotentials [85] and plane-wave basis set, and the starting wave functions were generated with the Perdew-Burke-Ernzerhof (PBE) [86] functional using the STATE code [87]. To calculate the correlation part of the GW self-energy, we evaluated the full frequency dependence of the dielectric function numerically, and the use of the plasmon-pole model is avoided. On the imaginary frequency/time axis, polarizability, dielectric function, screened Coulomb potential, and self-energy have smoothly decaying tails, which are fitted to simple model functions. The remaining energy/time region around zero is treated numerically. The matrix elements of the correlation self-energy on the imaginary time axis are fitted to a model function, followed by the fast Fourier transform to those on the imaginary frequency axis. Then, they are analytically continued onto the real energy axis [83].

In addition to the G_0W_0 calculation based on the PBE wave functions, we performed the eigenvalue-only self-consistent GW calculations (evGW) [88, 89], to check the starting point dependence [90–95] of the G_0W_0 calculations. In the evGW calculations, we considered only the diagonal part of the self-energy, and only the eigenvalues were updated in constructing the Green's function and the screened Coulomb potential, while we retained the wave functions unchanged (see Eqs. 4.2, 4.3, 4.4, 4.5, and 4.6), assuming that the starting DFT wave functions are close to the true quasiparticle wave functions [18, 96]. We updated the quasiparticle energies of up to the second lowest unoccupied band. To avoid explicitly calculating the quasiparticle energies of the bands whose number exceeds 1000 (see the number of empty states used in the calculation of the Green's function Eq. 4.3, as mentioned below) while retaining the accuracy of the calculated band energies around the conduction band edge, the energies of the higher bands outside the preset energy window were corrected by a scissors-like operation, that is, they were shifted rigidly by $\Delta = E_{m\mathbf{k}} - \varepsilon^{\mathrm{DFT}}_{m\mathbf{k}}$, where $E_{m\mathbf{k}}$, $\varepsilon^{\mathrm{DFT}}_{m\mathbf{k}}$ are, respectively, the quasiparticle energy and the DFT eigenvalue in the highest band m in the preset energy window. Here,

we chose second lowest unoccupied band. We found that five or six iterations were necessary to converge the fundamental gap within 0.01 eV.

For the GW calculations, we transformed the lattice vectors to employ the symmetry points and lines in the Brillouin zone defined in Ref. [97]. We used a $4 \times 3 \times 2$ (naphthalene, anthracene, and pentacene) or a $3 \times 2 \times 4$ (tetracene) Γ-centered **k**-point set, corresponding to the **k**-space mesh sizes of 0.19–0.43 $Å^{-1}$. For naphthalene, anthracene, and tetracene crystal, plane-wave cutoffs of 60 Ry and 24 Ry for the wave function and the dielectric matrix, respectively, were used [13]. For pentacene, we employed plane-wave cutoff of 40 Ry throughout the calculation, that is, for both the wave function and the dielectric matrix. We have found that the convergence of the calculated band gap or band width for the new set of cutoff is similar to that of the cutoff used in Ref. [13]. The number of empty states used in the calculation of the Green's function was 6006 (naphthalene), 5372 (anthracene), 6584 (tetracene), and 5200 (pentacene) bands, which encompass more than 240 eV above the center of the band gap. The convergence of the calculated band gap (band width) with respect to the number of empty states, **k**-point sampling, and plane-wave cutoff is estimated to be within 0.05 (0.01) eV.

Table 4.2 displays the calculated fundamental gap of oligoacene crystals within rev-vdW-DF2 and GW approximations. Figures 4.2a, 4.3a, 4.4a, and 4.5a show the calculated dispersions of the highest occupied (HOMO) and lowest unoccupied molecular orbital (LUMO)-derived bands of the oligoacene single crystals within GW. Because of the self-energy correction, the fundamental gap obtained with the one-shot GW (G_0W_0) was larger than the DFT values by 1.1–1.8 eV. The valence and conduction band widths became larger by the G_0W_0 self-energy correction by 0.05–0.15 eV and 0.04–0.12 eV, respectively [13]. The appreciable increase in band

Table 4.2 Calculated fundamental band gap (E_g) and band width for the HOMO-derived band (W_H) and that for the LUMO-derived band (W_L) of the oligoacene crystals obtained with rev-vdW-DF2 and GW based on the rev-vdW-DF2 optimized structures. The band gap average over the **k**-points in the Brillouin zone is shown in the parenthesis. The unit is eV. (Reprinted from [13], with the permission of AIP Publishing)

	Naphthalene	Anthracene	Tetracene	Pentacene
E_g(rev-vdW-DF2)	2.97	1.89	1.08	1.03
$E_g(G_0W_0)$	4.72 (5.01)	3.37 (3.67)	2.40 (2.75)	2.09 (2.38)
E_g(evGW)	5.70	4.17	3.09	2.68
E_g(Exp.[1])	5.0–5.5	3.9–4.2	2.9–3.4	2.2–2.4
W_H(rev-vdW-DF2)	0.44	0.40	0.44	0.74
$W_H(G_0W_0)$	0.51	0.46	0.49	0.89
W_H(evGW)	0.56	0.50	0.54	0.96
W_L(rev-vdW-DF2)	0.35	0.63	0.65	0.70
$W_L(G_0W_0)$	0.39	0.75	0.73	0.82
W_L(evGW)	0.41	0.78	0.75	0.86

[1] Refs. [71–80]

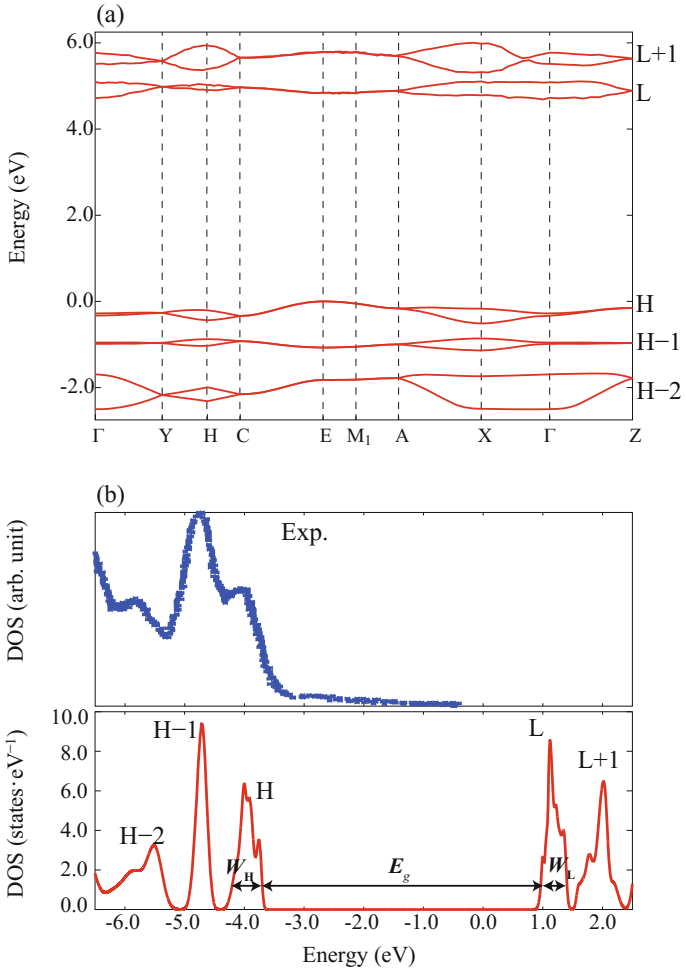

Fig. 4.2 (**a**) The band structure of the naphthalene crystal calculated within the G_0W_0 approximation. The energy zero is set to the top of the highest occupied band. The atomic configurations and the lattice constants are optimized with the rev-vdW-DF2 functional (Table 4.1). We transformed the lattice parameters to adopt the symmetry points and lines in the Brillouin zone defined in Ref. [97], to obtain a' =5.898 Å, b' =7.806 Å, c' =8.012 Å, α' =65.93°, and $\beta' = \gamma'$ =90.0°. The high-symmetry points in the BZ are Γ (0,0,0), Y(0,0,0.5), H(0, 0.361, 0.651), C(0, 0.5, 0.5), E(0.5, 0.5, 0.5), M_1(0.5, 0.639, 0.349), A(0.5, 0.5, 0), X(0, 0.5, 0), Z(0.5, 0, 0) in the unit of the basic reciprocal lattice vectors. (**b**) The density of states (DOS) based on the G_0W_0 band structure. The Gaussian broadening is set to the imaginary part of the self-energy obtained with the G_0W_0 calculation. The symbols such as H, H−1, L, and L+1 denote the molecular orbitals of the constituent molecules such as HOMO, next HOMO, LUMO, and the next LUMO, respectively, which forms the bands. For comparison, the experimental photoemission data (Ref. [81]) is displayed in the upper panel. The theoretical highest peak of the valence band maximum is aligned with that of the experimental photoemission peak by a rigid shift of the band energies. The band widths (W_H and W_L) and band gap (E_g) are indicated by the double-headed arrows for guides to the eyes. (Reprinted from [13], with the permission of AIP Publishing)

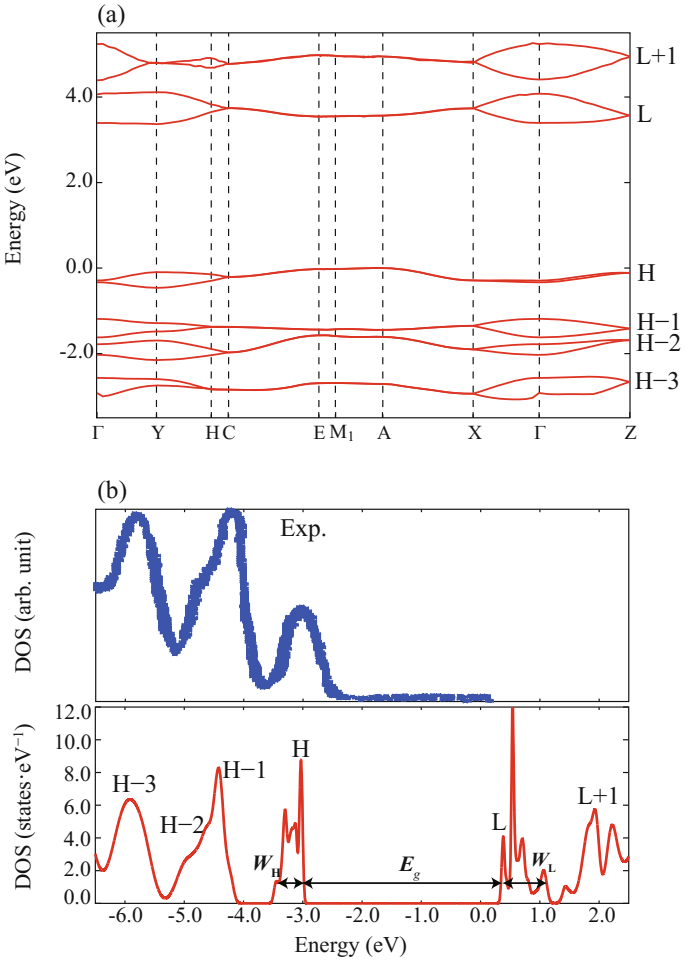

Fig. 4.3 (**a**) The band structure of the anthracene crystal calculated within the G_0W_0 approximation. The energy zero is set to the top of the highest occupied band. The atomic configurations and the lattice constants are optimized with the rev-vdW-DF2 functional (Table 4.1). We transformed the lattice parameters to adopt the symmetry points and lines in the Brillouin zone defined in Ref. [97], to obtain a' =5.948 Å, b' =8.339 Å, c' =9.242 Å, α' =78.00°, and $\beta' = \gamma'$ =90.0°. The high-symmetry points in the BZ are: Γ(0,0,0), Y(0,0, 0.5), H(0, 0.425, 0.598), C(0, 0.5, 0.5), E(0.5, 0.5, 0.5), M_1(0.5, 0.575, 0.402), A(0.5, 0.5, 0), X(0, 0.5, 0), Z(0.5, 0, 0) in the unit of the basic reciprocal lattice vectors. (**b**) The density of states (DOS) based on the G_0W_0 band structure. The experimental photoemission data (Ref. [81]) is displayed. The convention is the same as that in Fig. 4.2. The band widths (W_H and W_L) and band gap (E_g) are indicated by the double-headed arrows for guides to the eyes. (Reprinted from [13], with the permission of AIP Publishing)

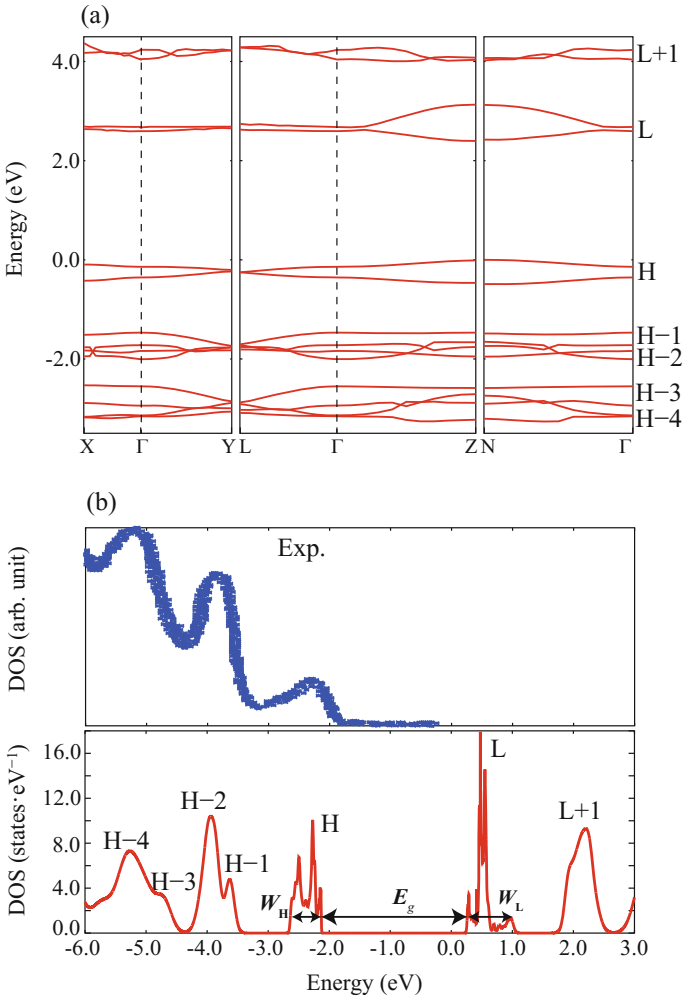

Fig. 4.4 (**a**) The band structure of the tetracene crystal calculated within the G_0W_0 approximation. The energy zero is set at the top of the highest occupied band. The atomic configurations and the lattice constants are optimized with the rev-vdW-DF2 functional (Table 4.1). We transformed the lattice parameters to adopt the symmetry points and lines in the Brillouin zone defined in Ref. [97], to obtain a' =7.686 Å, b' =12.489 Å, c' =6.019 Å, α' =99.62°, β' =94.36°, γ' =100.83°. The high-symmetry points in the BZ are X(0.5, 0, 0), Γ(0,0,0), Y(0, 0.5, 0), L(0.5, 0.5, 0), Z(0, 0, 0.5), N(0.5, 0, 0.5), M(0, 0.5, 0.5), R(0.5, 0.5, 0.5) in the unit of the basic reciprocal lattice vectors. (**b**) The density of states (DOS) based on the G_0W_0 band structure. The experimental photoemission data (Ref. [81]) is displayed. The convention is the same as that in Fig. 4.2. The band widths (W_H and W_L) and band gap (E_g) are indicated by the double-headed arrows for guides to the eyes. (Reprinted from [13], with the permission of AIP Publishing)

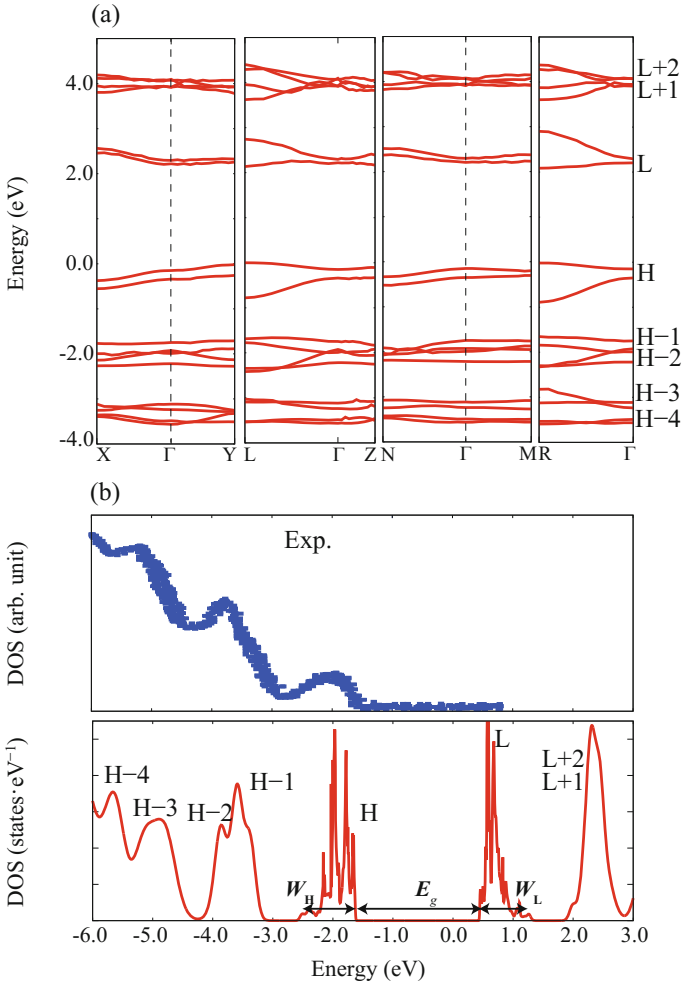

Fig. 4.5 (**a**) The band structure of the pentacene crystal calculated within the G_0W_0 approximation. The energy zero is set at the top of the highest occupied band. The atomic configurations and the lattice constants are optimized with the rev-vdW-DF2 functional (Table 4.1). The lattice parameters to adopt the symmetry points and lines in the Brillouin zone defined in Ref. [97] are the same as those in Table 4.1. The high-symmetry points in the BZ are X(0.5, 0, 0), Γ(0,0,0), Y(0, 0.5, 0), L(0.5, 0.5, 0), Z(0, 0, 0.5), N(0.5, 0, 0.5), M(0, 0.5, 0.5), R(0.5, 0.5, 0.5) in the unit of the basic reciprocal lattice vectors. (**b**) The density of states (DOS) based on the G_0W_0 band structure. The experimental photoemission data (Ref. [81]) is displayed. The convention is the same as that in Fig. 4.2. The band widths (W_H and W_L) and band gap (E_g) are indicated by the double-headed arrows for guides to the eyes

width suggests distribution of the electronic charge density at the intermolecular site, as indicated in Refs. [98–100].

Compared to the fundamental gap estimated with the experimental technique such as photoconductivity, optical absorption, and inverse photoemission measurements [71–80], the theoretical band gap within G_0W_0 is underestimated. The band gap averaged over the **k**-points in the Brillouin zone was also slightly underestimated, which is in line with Ref. [52]. To remove the starting point dependence of the G_0W_0 calculation [90–95], we took partially into account the effect of self-consistency within the eigenvalue-only self-consistent GW (evGW) treatment [88, 89]. As a result, the fundamental gap becomes slightly overestimated, becoming closer to experiments (see Table 4.2) [13]. For pentacene, the gap is in agreement with the recent experimental value measured with the low-energy inverse photoemission spectroscopy (LEIPS) [80]. The band widths slightly increased by the evGW calculation by at most 0.07 eV, independently of the **k**-point.

Figures 4.2b, 4.3b, 4.4b, and 4.5b display the calculated density of states (DOS) in comparison to the experimental photoemission measurement, in which the substrate temperature was kept at 150 K [81]. We calculated the DOS with the Gaussian smearing with the width set to the imaginary part of the self-energy obtained with the G_0W_0 calculation, rather than a uniform broadening. The width or the satellite peak structure of photoemission spectra is, in principle, the imaginary part of the self-energy, i.e., spectral function. Notice that according to Ref. [101], the structures of the organic thin films are similar to those of the single crystal investigated in this study, implying that comparison of the theoretical electronic structures of bulk organic crystals with the experimental photoemission spectra of organic thin films is meaningful. The calculated peak positions of the valence bands derived from HOMO, the next HOMO, the second next HOMO, and so forth, of the constituent molecule, are in agreement with the experimental photoemission spectra of the thin films on Ag(111) [81]. Some shoulder structures are found in the vicinity of the valence band, for instance, H-1 and H-3 DOS peaks in tetracene, which are not resolved in the experimental photoemission spectra. Although there is agreement found between the theoretical DOS and the experiment, factors affecting the experimental photoemission spectra of organic semiconductors such as broadening by temperature effects, instrumental resolution, and other factors causing structural disorder [102] should be taken into account. The incomplete charge screening at the surface was taken into account, when the G_0W_0 DOS of oligoacenes were compared with the experimental data [52]. Furthermore, it was proposed that the electron-phonon coupling and structural disorder should be taken into account to describe the electronic structure of organic semiconductors at finite temperature [103].

As far as the DOS of the unoccupied states are concerned, the inverse photoemission data of 2–3 monolayers of the oligoacenes on Ag(111) were reported [104]. The measured energy difference between the lowest and the second lowest unoccupied π^*-derived peaks was 0.8, 1.1, and 1.7 eV for naphthalene, anthracene, and tetracene, respectively [104]. The theoretical energy difference between the corresponding DOS peaks with G_0W_0 were 0.90, 1.39, and 1.73 eV, respectively, in fair agreement with the experiment.

4.2.1.3 Effects of the Crystal Geometry and the Molecular Configuration

Here, we investigated the impact of the different crystal structures on the electronic structure. For tetracene, theoretical DOS was obtained for the three crystal structures with different lattice constants (Table 4.3). Figure 4.6 displays the theoretical DOS of HOMO- and LUMO-derived bands for the different lattice constants. The calculated band gap and the band widths are summarized in Table 4.4. The experimental crystal geometry determined by the X-ray diffraction measurement [45, 46] and more recent diffraction data measured at 175 K [50] were used. We optimized their internal degrees of freedom with rev-vdW-DF2, while we fixed the

Table 4.3 Lattice constants of the tetracene crystals (Structures I–III) investigated. Structure III corresponds to the fully optimized crystal geometry, whose lattice constants were transformed, as described in the caption of Fig. 4.4. (Reprinted from [13], with the permission of AIP Publishing)

	a(Å)	b(Å)	c(Å)	α(°)	β(°)	γ(°)
Structure I[1]	7.980	12.747	6.140	100.44	92.5	101.92
Structure II[2]	7.837	12.552	6.056	99.45	94.20	101.27
Structure III[3]	7.686	12.489	6.019	99.62	94.36	100.83

[1]Ref. [45, 46, 53]. X-ray diffraction data whose temperature is presumed to be room temperature or higher
[2]Ref. [50]. X-ray diffraction data measured at 175 K
[3]This work

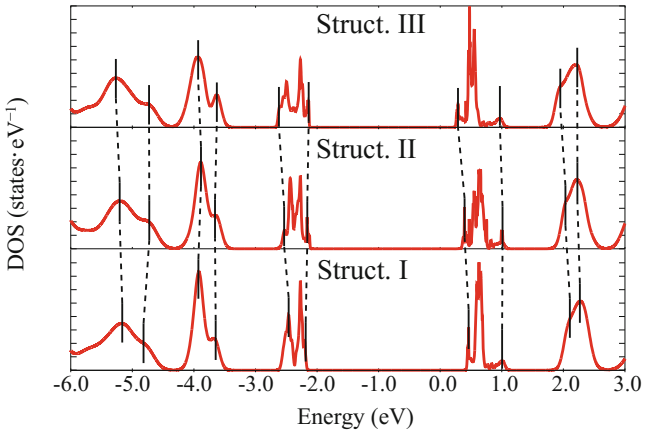

Fig. 4.6 The G_0W_0 densities of states (DOS) of tetracene obtained using different geometries. Structures I and II correspond to those obtained by the X-ray diffraction measurements (Refs. [45] and [50], respectively), where the internal atomic configurations were optimized with rev-vdW-DF2. Structure III was the fully optimized rev-vdW-DF2 structure reported in Table 4.1. The theoretical highest peaks of the valence band maximum in Structures I and II are aligned with that in Structure III. For the ease of comparison, we draw the solid vertical lines for the main peaks in the G_0W_0 DOS, and the states derived from similar molecular orbitals are connected by dashed lines. (Reprinted from [13], with the permission of AIP Publishing)

Table 4.4 Calculated band gap (E_g) and the band width for the HOMO-derived band (W_{H}) and that for the LUMO-derived band (W_{L}) of the tetracene crystal obtained with G_0W_0 and evGW for different structures. I and II denote the structures obtained by the X-ray diffraction experiment in Refs. [45] and [50], respectively, and their internal atomic coordinates were relaxed with their lattice constants fixed. Structure III denotes the one obtained by fully optimizing the cell and internal degrees of freedom, corresponding to the crystal geometry displayed in Table 4.1. E'_g is the molecular fundamental gap plus the polarization effect (see the main text). Unit is eV. (Reprinted from [13], with the permission of AIP Publishing)

Structure	I	II	III
$E_g(G_0W_0)$	2.63	2.50	2.40
$E_g(\mathrm{ev}GW)$	3.31	3.19	3.09
$W_{\mathrm{H}}(G_0W_0)$	0.39	0.45	0.49
$W_{\mathrm{H}}(\mathrm{ev}GW)$	0.44	0.48	0.54
$W_{\mathrm{L}}(G_0W_0)$	0.60	0.66	0.73
$W_{\mathrm{L}}(\mathrm{ev}GW)$	0.64	0.71	0.75
$E'_g(G_0W_0)$	3.12	3.06	3.01
$E'_g(\mathrm{ev}GW)$	3.85	3.79	3.74

lattice constants displayed in Table 4.3. We denote their structures by Structures I and II, for the former and the latter, respectively, and the structure fully optimized with rev-vdW-DF2 is denoted by Structure III.

It is found that the decrease in equilibrium volume from Structure I to III causes the band width to increase: The band width for the HOMO-derived band increases from 0.39 eV for Structure I (598.9 Å^3) to 0.49 eV for Structure III (556.0 Å^3). This is because the overlap between HOMOs of the neighboring molecular sites increases as the cell volume decreases. The result is similar to the change in the theoretical band widths, depending on the lattice constants of a variety of the experimental crystal structures of the organic semiconductors [105].

The fundamental gap also depends on the equilibrium volume. Table 4.4 shows that the band gap is narrowed as the volume decreases from Structure I to III. This is because of the dielectric screening stabilizing the electron or the hole injected into the bulk, which is induced by the surrounding polarization clouds. There is similar trend found in the result obtained at the evGW level of theory, in which the band energies are shifted almost independently of the **k**-points. The different polarization effect could be shown by the fundamental gap plus the polarization effect [80]. That was estimated by adding the halves of the band widths to the fundamental gap: $E'_g = E_g + (W_{\mathrm{H}} + W_{\mathrm{L}})/2$, to remove the effect of the change in the band width. As shown in Table 4.4, the calculated E'_g reasonably decreases as the cell volume increases.

To gain more insights into the effects of the molecular configuration on the electronic structure, we examined the electronic structures in terms of the interaction between the orbitals centered at the molecular sites. We obtained the maximally localized Wannier functions (MLWF) [14, 15] based on the PBE wave function for Structures I–III. We calculated the nearest-neighbor transfer integrals between the HOMOs or between the LUMOs arranged along the unit cell vectors ($t_{\mathrm{a1}} - t_{\mathrm{c1}}$ and

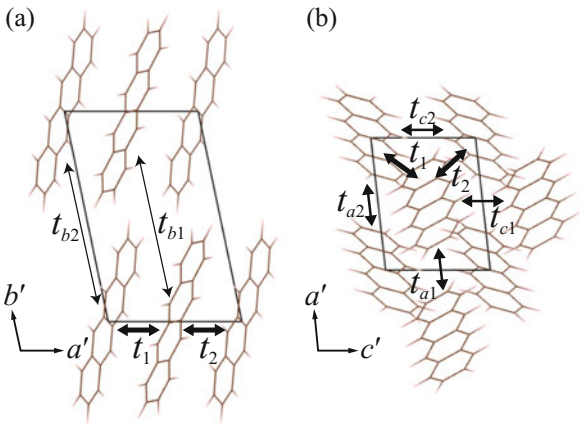

Fig. 4.7 Schematic views of the transfer integral between molecules projected on (**a**) $a'b'$ plane and (**b**) $a'c'$ plane. Conventional unit cell is shown. The unit cell vectors are the same as those defined in Fig. 4.4. (Reprinted from [13], with the permission of AIP Publishing)

$t_{a2} - t_{c2}$) and those along the diagonal directions between the two nonequivalent herringbone-stacked molecules in the cell (t_1 and t_2), which are depicted in Figs. 4.7 and 4.8. In Table 4.5, the transfer integrals for Structures I–III are shown, along with the HOMO- and the LUMO-derived band width determined with the tight-binding approximation. The tight-binding band structure for Structures I–III based on the calculated transfer integrals is displayed in Fig. 4.9.

It is found that the tight-binding band structure is in fair agreement with the first-principles band structure obtained with DFT-PBE. The result is in line with the previous works of oligoacene crystals [106–108]. The transfer integrals along the diagonal paths between the two nonequivalent molecules in the cell (t_1 and t_2) are largest in amplitude, crucially determining the band widths. The magnitudes of t_1 and t_2 for HOMO and LUMO and thus the band width increase from Structures I to III.

The isosurfaces of the MLWF for the two HOMOs and the two LUMOs of the two nonequivalent molecules in the unit cell are displayed in Fig. 4.8. The transfer integral t_1 for HOMO is dominated by the closest antibonding contribution to the interaction between the two HOMOs, resulting in largely positive values (see Table 4.5). On the other hand, t_2 for HOMO is negative, which originates from the closest in-phase bonding interaction. The distance between the molecules is an important factor dominating the transfer integrals and thus the HOMO-derived band widths. Actually, Structure III, with the smallest cell volume, displays the largest band width. In case of the LUMO band, the situations are similar.

However, with their nodal structures as shown in Fig. 4.8, there are competing bonding and antibonding contributions to the transfer integrals. Depending on the intermolecular distance or the molecular orientation angle, the signs of the transfer integrals can switch. The signs of t_1 and t_2 for HOMO switch even when the experimental crystal structures reported in Refs. [45] and [50] are, respectively, relaxed into Structures I and II, with only a minor change in the intermolecular distance or the molecular orientation angle [13]. We also found that the signs of

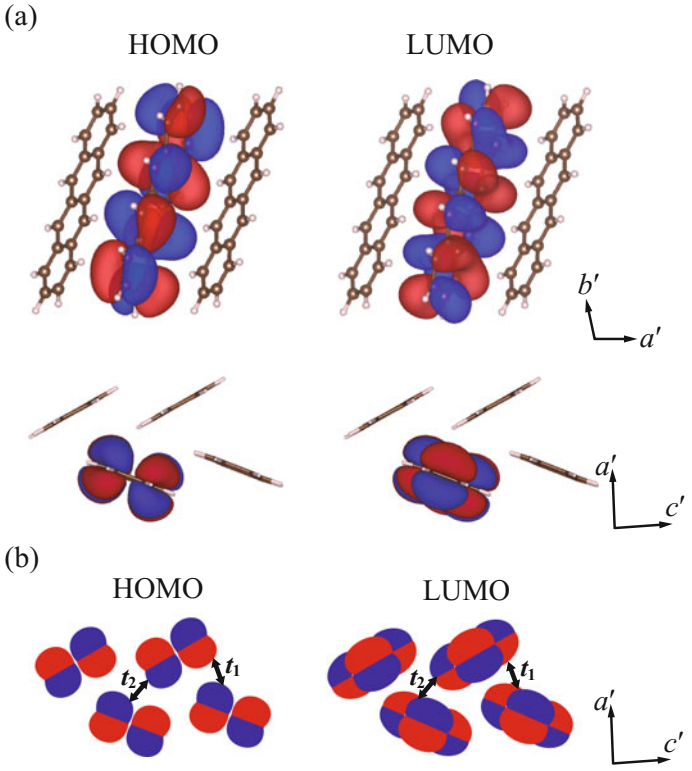

Fig. 4.8 (**a**) Isosurfaces of the maximally localized Wannier functions (MLWFs) corresponding to the HOMO and the LUMO located at one of the two nonequivalent molecules in the unit cell. Different colors (*brightness*) indicate signs of the orbitals. Views from the shortest cell vector c' (*upper*) and those from the longer molecular axis (*lower*) are shown. (**b**) Schematics of the transfer integrals t_1 and t_2 between the MLWFs of the HOMO (*left*) or the LUMO (*right*). The lattice vectors are the same as those defined in Fig. 4.4. (Reprinted from [13], with the permission of AIP Publishing)

the transfer integrals depend on the approximations in the first-principles DFT calculations (PBE or rev-vdW-DF2, in this case). The role of the molecular displacement along the slip direction determining the transfer integral was discussed [109]. In classifying the sign of the transfer integral between the herringbone-like arranged molecules of the pentacene polymorphs, the distance of the molecular slip stepping over the nodes of the molecular orbitals was taken into account [108]. In the present case, the switch of the signs of the transfer integrals t_1 and t_2 does not affect the band structure within the tight-binding approximation [13, 106–108]. Nevertheless, in general, a subtle interplay between the molecular configurations such as distance and angle, and their displacement, and, therefore, the accurate determination of the crystal geometry of organic crystals is crucial for predicting the electronic structure precisely.

Table 4.5 Calculated nearest-neighbor transfer integrals for the HOMO and those for the LUMO of the tetracene crystal obtained with the maximally localized Wannier functions [14, 15] based on the DFT-PBE orbitals. t_{c1} and t_{c2} correspond to the transfer integrals along the shortest unit cell vector, t_{a1} and t_{a2} to those along the second shortest unit cell vector, and t_1 and t_2 to those between the two nonequivalent tetracene molecules as depicted in Figs. 4.7 and 4.8 (t_{b1} and t_{b2} along the longest cell vector are found to be essentially zero). $W_{\mathrm{H}}^{\mathrm{TB}}$ ($W_{\mathrm{L}}^{\mathrm{TB}}$) and $W_{\mathrm{H}}^{\mathrm{PBE}}$ ($W_{\mathrm{L}}^{\mathrm{PBE}}$) denote the HOMO (LUMO)-derived band width within the tight-binding approximation and the first-principles calculation with DFT-PBE, respectively. I and II denote the structures obtained by the X-ray diffraction experiment in Refs. [45] and [50], respectively, and their internal atomic coordinates were relaxed with their lattice constants fixed. Structure III denotes the one obtained by full optimization of the cell and internal degrees of freedom, corresponding to the crystal geometry displayed in Table 4.1. Unit is meV. (Reprinted from [13], with the permission of AIP Publishing)

Structure	I	II	III
	HOMO		
t_{c1}	12.39	11.37	12.15
t_{c2}	−4.72	−6.95	−6.48
t_{a1}	−2.74	−4.33	−5.19
t_{a2}	−2.23	−3.08	−3.22
t_1	16.56	20.45	22.79
t_2	−60.43	−66.54	−78.39
$W_{\mathrm{H}}^{\mathrm{TB}}$	313.35	355.34	411.43
$W_{\mathrm{H}}^{\mathrm{PBE}}$	322.17	370.68	417.33
	LUMO		
t_{c1}	−31.01	−31.10	−33.04
t_{c2}	−11.13	−10.76	−12.10
t_{a1}	−1.55	−1.74	−2.09
t_{a2}	−3.43	−4.09	−4.74
t_1	68.44	73.62	81.07
t_2	−57.38	−67.96	−78.02
$W_{\mathrm{L}}^{\mathrm{TB}}$	510.78	570.12	639.72
$W_{\mathrm{L}}^{\mathrm{PBE}}$	505.09	563.99	629.19

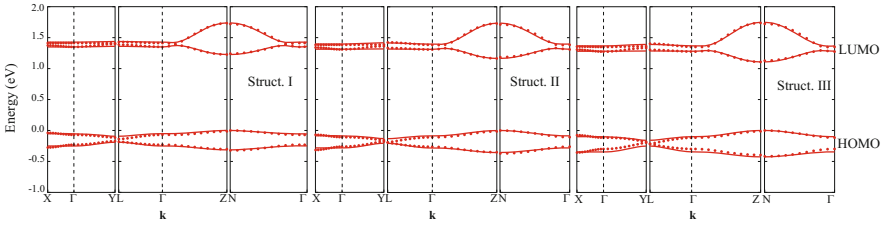

Fig. 4.9 Band structure of the tetracene crystals (Structures I–III). HOMO- and LUMO-derived bands are displayed. Solid lines indicate the band structure within the tight-binding approximation based on the transfer integrals calculated with the maximally localized Wannier functions (see Table 4.5). Dots indicate the band structures obtained with the first-principles DFT-PBE calculation. (Reprinted from [13], with the permission of AIP Publishing)

4.2.2 *Electronic Properties at Organic-Metal Interfaces: Energy Level Alignment and Emergence of the Image Potential-Like States*

The important physical phenomenon crucially affecting the energy level alignment at the interface and thus the charge transport properties [110] is the renormalization of the HOMO-LUMO energy gap induced by the metal surface [111–113]. When a molecule is close to the metal surface, electrons in the metal respond to and screen charged excitations of the molecule. The molecular energy levels at the interface are thus quasiparticle energy levels. As a result, when the molecule is located close to the metal surface, the molecular HOMO and LUMO levels shift closer to the metal Fermi level, and the HOMO-LUMO fundamental gap is narrowed [111–113]. A rigorous theoretical treatment is the many-body perturbation theory within the GW approximation for accurate treatment of the quasiparticle energies at the organic-metal interface [112, 113]. However, the computationally demanding GW treatment hampers its application to periodic systems with hundreds of atoms even with present-day computational resources. That is also the case in treatment of an organic-metal interface by employing a periodic slab model with a vacuum layer along the direction normal to the slab [114]. In addition to the system size tractable, the numerical convergence of the molecular quasiparticle energies and the metal work function can be a problem [114, 115]. The DFT wave functions can be poor approximations to the quasiparticle wave functions for hybridized interfaces, which necessitate diagonalization of the self-energy matrix $\Sigma(\mathrm{E})$ for a better new starting point for the perturbation beyond G_0W_0 or another computational strategy such as evaluation of the self-energy in the basis of the molecular orbitals, which is expected to be diagonal [114].

To avoid the technical issues involved in the GW calculation of the overall interface system, some efforts have been made, for instance, the DFT+Σ approach [112, 116]. For physisorbed systems, with the assumption of weak coupling between the molecule and the metal, the PDOS peaks of an isolated molecule could be shifted by the quasiparticle self-energy correction to HOMO and LUMO energies, along with the gap renormalization upon adsorption on the metal. With DFT+Σ, one adds two corrections denoted by Σ to HOMO-/LUMO-derived levels obtained with DFT within LDA or GGA. First, a difference between HOMO or LUMO energy of an isolated molecule with DFT-LDA or DFT-GGA and that obtained at a highly accurate level of theory such as GW is estimated. Second, the polarization at the surface inducing gap renormalization is corrected based on the classical image charge model $1/4[z - z_0]$, where z is the average height of the molecule on the surface and z_0 is the image plane position. The DFT+Σ method has been successfully employed to predict or elucidate the energy level alignment at organic-metal interfaces with physisorption [112, 117] and to explain the charge transport in molecular junctions where the assumption of weak coupling is reasonable [116].

Overall, however, the representative theoretical works calculating the energy level alignment at organic-metal interfaces within GW or DFT+Σ, despite its

rigorous theoretical background, have been limited to the abovementioned works [112–117]. The computational or numerical difficulty involved, as mentioned above, seems to be a critical limiting factor. Furthermore, determination of the quasiparticle wave functions in a self-consistent manner is necessary in case of a hybridized interface involving appreciable charge transfer at the interface. In terms of the modification of the electronic charge density at a hybridized organic-metal interface in a self-consistent manner, a theoretical methodology within the framework of DFT, such as the optimally tuned range-separated hybrid (OT-RSH), might be a method of choice [118–120].

Unoccupied electronic states at surfaces and interfaces are important as they are relevant to the charge carrier transport in the electronic devices. As such, the image potential state (IPS) is a fundamental electronic state emerging at metal surfaces, which is characterized by a set of Rydberg-like series induced by the Coulombic tail of the potential [121, 122]. Image potential has a form of $V_{\mathrm{im}} = -e^2/4(z - z_0)$, where z_0 is the position of the so-called image plane, the effective position of the surface plane, and the energy levels in the image potential is given by $E_n = -0.85\,\mathrm{eV}/(n + a)^2$ with n and a being the quantum number and the so-called quantum defect, respectively. The IPSs have been shown to exist even for graphitic materials including single-crystal graphite [123], highly oriented pyrolytic graphite [124], carbon nanotube [125], fullerene [126], and fullerite [127]. Double Rydberg states of IPSs are also predicted for freestanding graphene [128] by using the LDA augmented by the image potential tail ("LDA+image tail"), and it was suggested that the IPS is the origin of the interlayer state [nearly free electron (NFE) state] of graphite [129–131]. The double Rydberg states were confirmed for graphene and bilayer graphene on SiC by using the scanning tunneling spectroscopy [132]. Computationally however, it is well-known that the semilocal approximation to the exchange-correlation functional fails to reproduce the image potential, and the dynamic and nonlocal correlation is necessary to describe it accurately. Indeed it has been shown that by using the GW method to evaluate the energy-dependent electron self-energy, an image potential for a metal surface is reproduced [133]. As an alternative, vdW-DF has been used to study graphene and some graphite materials [134], as it contains a dynamical and nonlocal piece of correlation in an approximate manner. In the following, electronic structures of graphitic materials obtained by using vdW-DF are discussed with the emphasis on the IPSs.

In Fig. 4.10, the band structure of graphene obtained by using the rev-vdW-DF2 [10] functional is shown [134]. It is in good agreement with that obtained with the LDA+image tail potential of Ref. [128]. In particular, the low-lying IPS levels agree well (Table 4.6), suggesting that vdW-DF improves the description of graphene's IPS. In order to clarify the role of the nonlocal correlation, calculations without the nonlocal correlation [B86R exchange plus PBE correlation (B86Rx+PBEc) and B86R exchange plus PBEsol correlation (B86Rx+PBEsol$c$)] were performed. It was found that the IPS levels obtained with B86Rx+PBEc and B86Rx+PBEsol$c$ are similar to those with PBE and underestimated, suggesting that the nonlocal correlation plays an important role in describing IPSs accurately. By further analyzing the exchange-correlation potential, it was found that the vdW-DF generates

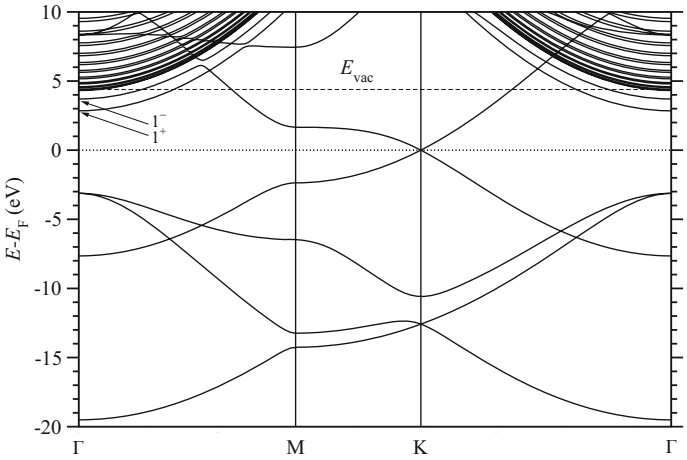

Fig. 4.10 Band structure of graphene obtained by using the rev-vdW-DF2 functional. The origin of energy is the Fermi level (E_F). The symmetry points are $\Gamma = (0, 0)$, $M = (1/2, 0)$, and $K = (1/3, 1/3)$ in the unit of the basic reciprocal lattice vectors. The horizontal dashed line indicates the vacuum level (E_{vac}). The low-lying IPSs corresponding the symmetric (1^+) and antisymmetric (1^-) are indicated by the arrows. (Reprinted from [134], with the permission of AIP Publishing)

Table 4.6 IPS levels of graphene with respect to the Fermi level calculated with rev-dW-DF2 along with those with LDA, PBE, and LDA+image tail ($z_o = 3.0$ Bohr). For comparison those obtained with B86Rx+PBEc and B86Rx+PBEsol$c$ are also shown. IPS levels with respect to the vacuum level are shown in parentheses. The rev-vdW-DF2 lattice constant was used for all the calculations. The unit of the energy level is eV. (Reprinted from [134], with the permission of AIP Publishing)

Method	1^+	1^-	2^+	2^-
rev-vdW-DF2	2.85 (−1.54)	3.70 (−0.69)	4.31 (−0.07)	4.35 (−0.04)
LDA	3.31 (−1.16)	4.25 (−0.23)	4.41 (−0.07)	4.46 (−0.02)
PBE	3.27 (−0.98)	4.03 (−0.22)	4.24 (−0.01)	4.29 (+0.04)
B86Rx+PBEc	3.42 (−0.82)	4.00 (−0.24)	4.18 (−0.06)	4.23 (−0.01)
B86Rx+PBEsol$c$	3.42 (−0.89)	4.05 (−0.25)	4.25 (−0.05)	4.30 (+0.02)
LDA+image tail[a]	2.94 (−1.47)	3.69 (−0.72)	4.16 (−0.25)	4.22 (−0.19)

[a]Ref. [128]

more attractive and longer-range potential than PBE one. It was also found that the exchange potentials used in the improved vdW-DFs such as optB86b-vdW, vdW-DF-cx, and rev-vdW-DF2 are more attractive and longer ranged than PBE

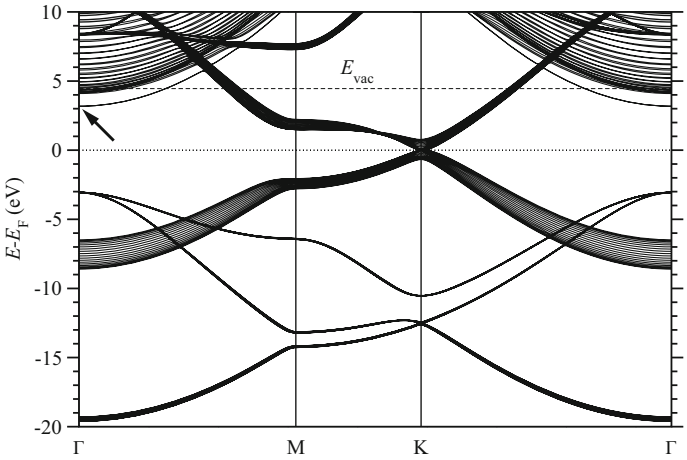

Fig. 4.11 Band structure of the graphite (0001) surface calculated by using rev-vdW-DF2. The origin of energy is E_F. The horizontal dashed line indicates E_{vac}. The lowest IPS is indicated by the arrow. (Reprinted from [134], with the permission of AIP Publishing)

exchange-correlation potential, and the attractive nonlocal correlation further gives more attractive exchange-correlation potential, resulting in the improved description of IPSs.

The band structure of the graphite (0001) surface was also calculated (Fig. 4.11), and the lowest IPS was obtained in the bulk band gap. The position of the lowest ($n = 1$) IPS obtained with rev-vdW-DF2 is 3.18 (-1.28) eV with respect to the Fermi level (vacuum level) and the second lowest ($n = 2$) IPS, 4.18 (-0.28) eV, while the lowest IPS obtained with PBE is 3.61 (-0.69) eV and the second IPS, 4.18 (-0.28) eV. Calculated IPSs with rev-vdW-DF2 are lower (deeper) than the energy of a Rydberg-like series $E_n = -0.85\,\text{eV}/(n+a)^2$ with small quantum defect a reported experimentally, and apparently those with PBE are in better agreement with the experiments. This is presumably because of the error cancellation between the derivative discontinuity and the image potential in PBE. vdW-DF also lacks the derivative discontinuity but gives more attractive nonlocal correlation energy and potential, thereby overestimating the magnitude of the IPS levels. Nevertheless, although the bulk energy gap and the energy levels of the unoccupied orbitals of gas-phase molecules are underestimated, they are described reasonably well on metal surfaces even with semilocal and vdW-DF functionals, and thus we expect the interaction between IPSs and unoccupied molecular orbitals on a metal surface is described fairly well with vdW-DF.

Here it is worth mentioning that there is also a considerable difference in the work function obtained with GGA and vdW-DF: Calculated work functions of graphene are 4.39 eV with rev-vdW-DF2 and 4.25 eV with PBE. Those of graphite are 4.46 eV with rev-vdW-DF2 and 4.30 eV with PBE at the rev-vdW-DF2 optimized geometry, and the former is in better agreement with the experimental value of 4.5–4.7 eV than the latter. Work function predicted by rev-vdW-DF2 is also in good agreement

with that obtained with optPBE-vdW [135]. These results indicate that the nonlocal correlation also affects the electronic structure, although its effect has been thought to be minor [136]. This is in line with the recent work by Ferri et al. [137] using the fully self-consistent Tkatchenko-Scheffler vdW correction [138].

IPSs of metal surfaces functionalized with molecular overlayers have also been investigated [132, 139–142]. Naphthalene on highly oriented pyrolytic graphite (HOPG) is one of prototypical systems for aromatic hydrocarbons physisorbed on a metal surface, and there have been several studies investigating its electronic properties [20, 143–146]. The scanning tunneling microscopy (STM) measurement revealed that the naphthalene overlayer on HOPG forms a superstructure with a tilted adsorption configuration [145]. Furthermore, based on the angle-resolved two-photon photoemission spectroscopy measurement, the authors of Ref. [145] suggested that the lowest IPS behaves almost like a free electron, despite the presence of the molecular overlayer [20].

To gain insights into the nature on the IPS at organic-metal interfaces, DFT calculations were conducted for naphthalene adsorbed on graphene [19]. The rev-vdW-DF2 functional [10] was used to correctly describe the molecule-substrate and the intermolecular interactions, which are typically of the vdW interaction nature. It was found that the naphthalene molecules are stabilized as a superstructure with a periodicity of $(2\sqrt{3} \times 2\sqrt{3})$ with a tilted molecular adsorption geometry, in good agreement with the STM measurement [145]. The band structure of the naphthalene/graphene was calculated (Fig. 4.12), and IPS-like states are found at 2.77 and 3.80 eV with respect to the Fermi level at the Γ point, which are characterized by anisotropic effective mass due to the anisotropic molecular configuration of the naphthalene overlayer. Further, by analyzing the corresponding charge densities of these states as shown in Fig. 4.13, it was found that these IPS-like states are formed

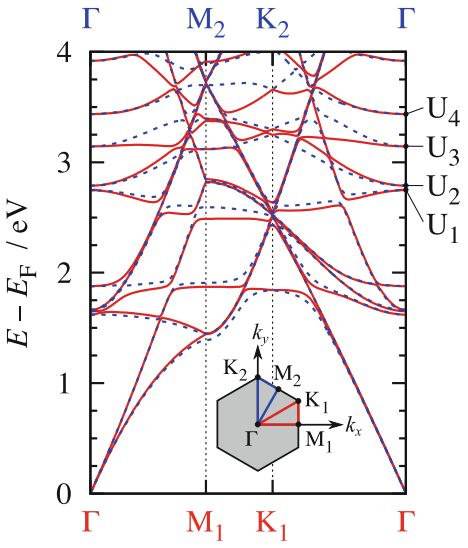

Fig. 4.12 Band structures for the unoccupied states for the naphthalene overlayer on graphene with $(\sqrt{3} \times \sqrt{3})$ periodicity. Energy zero is set to the Fermi level (E_F). The surface Brillouin zone is displayed in the inset

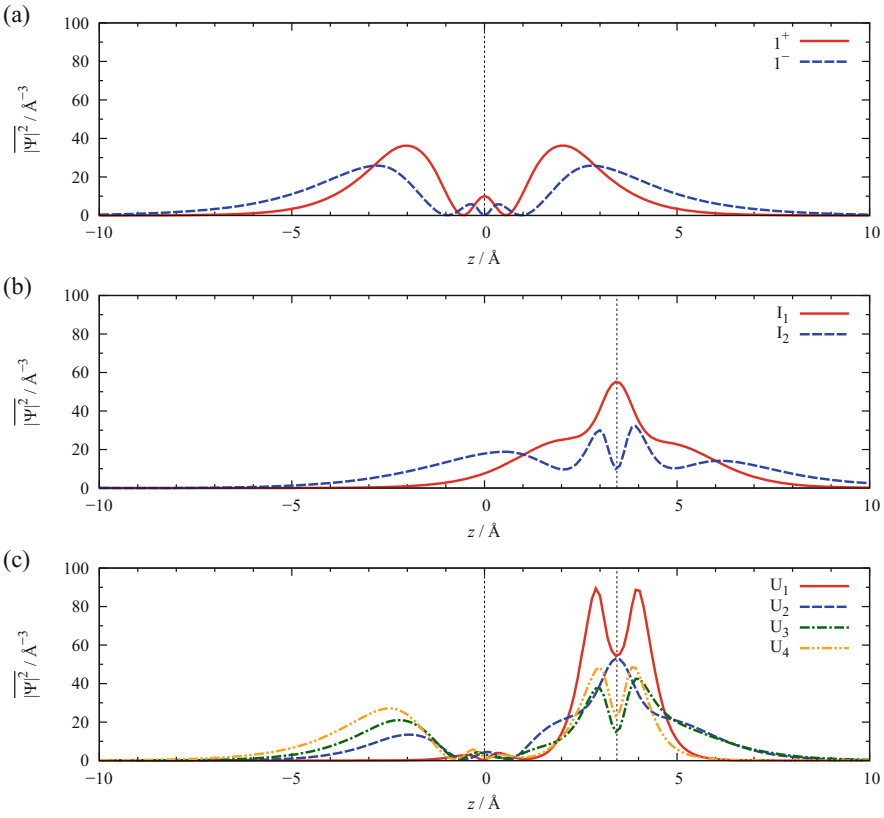

Fig. 4.13 Planer average of charge densities for (**a**) the graphene IPSs with even (1^+) and odd (1^-) parities, (**b**) the IPS-like states of naphthalene with even (I_1) and odd (I_2) parities, and (**c**) the unoccupied states of naphthalene on graphene

by the hybridization of the IPS of graphene and that of naphthalene, which originates from the Rydberg state of naphthalene molecule. In particular, the IPS-like state at 2.77 eV is the bonding state of the lowest IPS of graphene with the even parity and the IPS of naphthalene overlayer, and it was suggested that what is observed in the STM image [20] is this IPS-like state, not the molecular orbital-derived state as suggested before [20]. The results indicate that such "hybrid IPS" can be observed in a variety of systems, as IPS-like states, also known as nearly free electron states, are predicted not only for metal surfaces but also for semiconductors [147, 148], insulators [149, 150], and carbon-based nanostructures [126, 127, 151–157], and further experimental investigation on the IPS of different interfaces is anticipated. Here we stress that to predict the interface IPSs precisely, it is very important to describe the interface structures very accurately, and the use of vdW-DF is decisively important.

4.2.3 Theoretical Determination of the Ionization Energy and Electron Affinity

Energies of the valence and conduction band edges relative to the vacuum level of an organic molecular solid give the ionization energy (IE) and electron affinity (EA), quantities of primary importance leading to the energy levels of the injected or transported electron/hole at the organic-(in)organic heterojunction or inside the organic layer. Essentially, IE and EA are defined as follows:

$$\mathrm{IE} = \epsilon_{\mathrm{vac}} - \epsilon_{\mathrm{H}}, \mathrm{EA} = \epsilon_{\mathrm{vac}} - \epsilon_{\mathrm{L}}, \tag{4.7}$$

where ϵ_{vac} is the vacuum level and ϵ_{H} (ϵ_{L}) is the edge of the highest (lowest) occupied (unoccupied) energy level. Although the definition is straightforward for a molecule in a gas phase, there are physical effects to take into account in case of a molecular solid. The energy of the charge injected into the solid is renormalized: the particle is stabilized by the surrounding polarization clouds with opposite charge. The reduction in energy relative to the gas phase is referred to as polarization energy [158]. The polarization energy is formally described as

$$P^{+} = \mathrm{IE}_{\mathrm{g}} - \mathrm{IE}_{\mathrm{s}}, P^{-} = \mathrm{EA}_{\mathrm{s}} - \mathrm{EA}_{\mathrm{g}}, \tag{4.8}$$

where subscripts s and g denote solid and gas phases, respectively, and P^{+} (P^{-}) is the polarization energy upon injection of hole (electron). P^{+} corresponds to increase in energy of the electron in a solid, leading to reduction in IE relative to that in a gas phase, and vice versa in case of the polarization energy upon electron (P^{-}), resulting in the increased EA. Measurement or quantification of the polarization energy in organic solids dates back to the paper published by Sato, Seki, and Inokuchi in 1981, which was based on the comparison of the photoelectron spectroscopy data between the solid phase and the gas phase [158]. The measured polarization energies upon the injected hole in the solids (P^{+}) were reported to be in the range 0.9–3.0 eV [158]. The sum of the polarization energies $P^{+} + P^{-}$, corresponding to renormalization of the fundamental gap, becomes significant.

The reduced gap in the solid, inherently dielectric response event, may be captured with the theoretical methodologies such as the GW approximation, which describes the screened Coulomb potential based on the frequency-dependent microscopic dielectric function [112, 159]. The weak intermolecular interaction in organic solids may lead us to insights into the electronic nature described by a single molecule surrounded by a dielectric medium of the other molecules. Actually, treatment of a single molecule in the polarizable continuum model (PCM) or the quantum mechanics (QM)/molecular mechanics (MM) treatment gave reasonable estimation of IE and EA as total energy difference between neutral and charged systems obtained at the DFT-GGA level of theory [160, 161].

In photoemission measurements, the energy of the particles injected or extracted at the surface is measured, which is affected by the morphology or the molecular

orientation at the surface. As mentioned in the previous subsection, a rigorous theoretical method describing quasiparticle energy, for instance, GW approximation, requires fairly large computational resources, thus rendering difficult the application of the methodologies to a surface or an interface represented by a periodic slab model with a sufficiently thick vacuum layer.

To circumvent the computational difficulty, it was proposed recently that the electrostatic potential represented by a slab model within DFT-GGA approximation could be aligned to the electrostatic potential determined for a bulk system within the GW approximation [21]. The valence and conduction band edge energies (or HOMO- and LUMO-derived energies) of the bulk determined at the GW level of theory could be shifted according to the electrostatic potential of the surface slab model, for which a well-defined vacuum level could be determined. Overall, the resulting IE and EA are in fair agreement with experiments. The slightly smaller band gap than the experimental values may be ascribed to the different polarization effects in bulk and surface.

According to Ref. [80], $\mathrm{IE_s}$ and $\mathrm{EA_s}$ measured in photoemission or inverse photoemission experiments can be defined as

$$\mathrm{IE_s} = \mathrm{IE_g} - P^+ - \Delta^+, \mathrm{EA_s} = \mathrm{EA_g} + P^- + \Delta^-, \tag{4.9}$$

$$P^+ = E_p^+ + W^+, P^- = E_p^- + W^-, \tag{4.10}$$

where the terms Δ^+ and Δ^- correspond to the width of the valence and the conduction band edges, respectively, which are theoretically estimated with the first-principles band structure calculation. E_p^+ and E_p^- describe the induced polarization upon the injected hole and electron, respectively, which are approximately the same, because they are proportional to the square of the injected charge. On the other hand, W^+ and W^- denote the electrostatic interaction upon the injected hole and electron, respectively, which are different in sign but approximately the same in magnitude, because they are linear functions of the excess charge [162]. The electrostatic interaction W induced upon two-dimensional (2D) periodical arrangement of the molecules could be estimated by the difference in energy level between the isolated gas-phase molecule and the 2D periodically arranged molecules calculated within DFT-LDA or DFT-GGA, given the "nearsightedness" of the local chemical environment of the molecule [163, 164].

The IE and EA of the organic semiconductor thin films were theoretically obtained by adding to the gas-phase IE and EA the electrostatic terms W^+ and W^-, respectively, which are dominated by the long-range electrostatic interaction such as the charge-quadrupole interaction and depend on the surface molecular orientation [165], and the polarization-induced term E_p, which was assumed to be common for the injected hole and charge and thus was estimated as half the fundamental gap difference between the gas phase and the bulk [22]. The result for pentacenequinone, a pentacene derivative, is in agreement with the experimental measurement, demonstrating the molecular orientation crucially affecting the IE

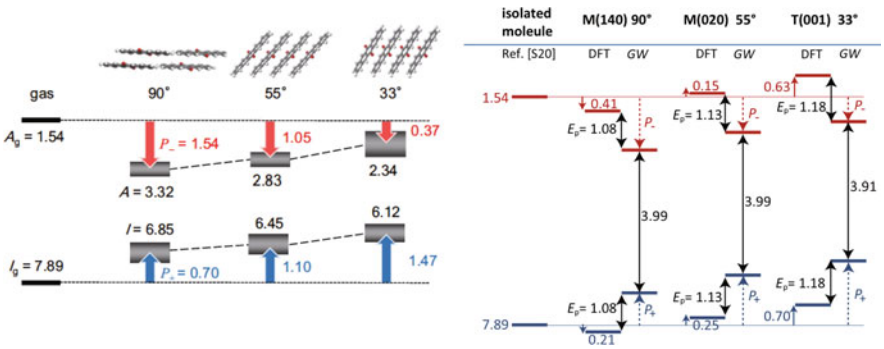

Fig. 4.14 Schematics on theoretical determination of the polarization energies P^+ and P^- (*right panel*) of pentacenequinone, in comparison to the low-energy inverse photoemission spectroscopy (LEIPS) measurement (*left panel*) in Ref. [22]. In the right panel, the solid one-headed arrows indicate the electrostatic term W^+ and W^-, and the double-headed arrows indicate the fundamental gap obtained within GW or the resulting induced polarization effect E_p. (Reprinted figure with permission from [22] Copyright 2018 by the American Physical Society)

and EA of the organic semiconductor [22] (see Fig. 4.14). The theoretical approach might play a role in prediction and tuning of the charge injection levels of organic semiconductors.

The theoretical approaches based on the periodic implementation of the GW approximation give important information on the impacts of the morphology or the molecular orientation at the surface on the charge injection levels. Nevertheless, the screening effect reduced at the surface should be taken into account. The QM/MM-based GW approach was proposed to treat quasiparticle energy of a molecular crystal, with the QM part treating the quasiparticle energy of a single molecule within GW, along with the MM part describing the effect of the surrounding molecules treated with the discrete polarizable model [23]. Based on a Gaussian atomic orbital-based implementation of GW [91] for the QM part, the response of the surrounding medium to the charged excitation of the molecule was described by the charge response model [166]. In addition to the many-body correlation and the polarization effects as taken into account within GW, crystal field effects were included at the stage of the starting DFT calculation, thus leading to the estimation of the charge injection levels relative to the vacuum level [23]. The resulting fundamental gaps of the crystals of pentacene and perfluoropentacene demonstrated the reduced polarization effect at the surface, i.e., the gap enlarged by $\approx 0.2\,\mathrm{eV}$ relative to the bulk. The crystal field effect induced rigid positive (negative) shift of the HOMO and LUMO levels for pentacene (perfluoropentacene), which the authors ascribed to the different charge-quadrupole interaction depending on the macroscopic shape of the surfaces [23, 167].

The results as mentioned above demonstrate that it is becoming possible to extract the physical ingredients dominating the charge injection barrier at an organic semiconductor surface in a quantitative manner.

4.3 Conclusions and Outlook

In this review, we have outlined recent theoretical works on basic electronic properties of organic semiconductors relevant to organic electronic devices with first-principles electronic structure methods. Firstly, we have demonstrated the performances of recently proposed van der Waals (vdW)-inclusive methods in prediction of crystal structures of the oligoacene crystals. It was found that a variant of the vdW density functional (vdW-DF) [10], with its reasonable computational cost being comparative to that of DFT-LDA or DFT-GGA, predicted the lattice constants in good agreement with the experimental values obtained with the diffraction data measured at low temperatures [13]. For the optimized crystal geometries, the many-body perturbation theory within the GW approximation [12, 18] predicted the fundamental band gap and the density of states in agreement with experiments. More importantly, different polarization energies were obtained for the different cell volumes measured at different temperatures, corresponding to the different molecular packing densities and thus the different screenings. Furthermore, based on the maximally localized Wannier functions (MLWF) [14, 15], the impact of the molecular configurations in the unit cell on the transfer integrals between molecules at the neighboring sites was discussed. The result demonstrates the subtle interplay between the intermolecular configurations such as distance and angle, and their displacement, and, therefore, the importance of predicting accurate geometry of organic semiconductor crystals is underscored [13]. Prediction of the crystal geometry of organic semiconductors and calculation of the MLWF, and thus the resulting intermolecular transfer integrals, may lead to multi-scale real-time simulation of the carrier transport in organic crystals [16]. With the aid of the present-day machine learning and artificial intelligence, a theoretical tool for automatic and efficient high-throughput screening of organic semiconductor materials might be realized in the near future.

Secondly, we discussed theoretical treatment of electronic phenomena in organic-metal interfaces. As an example of theoretical study on the interface energy level alignment, we summarized the works based on the GW approximation. GW approximation allows rigorous theoretical treatment of the charged excitation (quasiparticle) at the interface. Actually, there have been works successfully applying the same methodology to the energy level alignment at the physisorbed or hybridized interface. In consideration of the molecular gap renormalization at physisorbed interfaces dominated by the image potential, an approximated approach of adding the image potential effect $1/4z$ to the fundamental gap of an isolated molecule is found to be valid (DFT+Σ) [112, 116, 117]. However, the large computational cost which formally scales as N_{PW}^4 [168], where N_{PW} is the number of plane-wave basis set, the poor convergence of the quasiparticle energies including the work function of the metal, and the effect of self-consistency required [114, 115] critically prohibit one from applying the methodology to organic-metal interfaces in general. In terms of the effect of self-consistency, another formalism within the framework of DFT such as the optimally tuned screened range-separated hybrid (OT-SRSH) can be a method of choice [118–120].

Understanding of unoccupied states including image potential state (IPS) at organic-metal interfaces is of importance, and experimental or theoretical insight into prototype systems such as physisorption of a typical aromatic hydrocarbon on a graphite surface is required. Theoretically, GW approximation is one of the most promising electronic structure methods [169], because of its rigorous description of the long-ranged tail of the (screened) Coulomb potential. However, as far as the authors know, there is no report at present successfully investigating the IPS at organic-metal interfaces based on the same methodology, possibly because of the numerical or technical difficulty, as mentioned above. The approach based on a variant of vdW-DF may be a method of choice at present to gain insights into the IPS at organic-metal interfaces, with its long-range nature of the potential and accuracy in prediction of the interface geometry, along with its reasonable cost almost comparable to DFT-LDA or DFT-GGA [19, 134].

Thirdly, we have outlined recent theoretical approaches for determination of energy levels for charge injection, i.e., ionization energy (IE) and electron affinity (EA), at an organic semiconductor surface, which essentially determines barrier for charge injection. As with the previous topics, GW approximation is promising also for this problem. However, to avoid the numerical or technical difficulties involved in treatment of surfaces and interfaces with the periodic slab, there are some treatments proposed [21, 22], in which the vacuum level is determined based on the calculation of the slab model within DFT-GGA. The approach proposed in Ref. [22] successfully elucidated the dependence of the ionization energy and electron affinity on the surface morphology or the molecular orientation at the surface as measured by the LEIPS technique [170–172]. Nevertheless, in these approaches, the induced polarization effect in the bulk was treated. To be more quantitative in comparison to experimental measurements, the polarization effect on a surface should be taken into account, which is weaker than that in the bulk. A recently proposed approach based on QM/MM, in which IE and EA of a single molecule are treated at the GW level of theory, while the surrounding molecules are treated as continuum of dielectric medium, and thus the macroscopic shape of the surface can be treated within MM [23]. The result demonstrates quantitative treatment of IE and EA taking into account the presence of the organic crystal surface [23]. As far as the theoretical treatment of IE and EA of organic single crystals or thin films is concerned, this treatment may be a method of choice at present.

The first-principles theoretical methods, as outlined in this article, have allowed precise determination or prediction of the intrinsic basic electronic properties of organic semiconductor materials measured or observed in recent well-defined experimental measurements. Compared to the vast amount of database available and the understanding on the electronic properties of inorganic semiconductor materials, there is much room for understanding the basic electronic origin of the materials properties, and there is much need for constructing database for organic semiconductor materials. The roles of the first-principles electronic structure methods as described here, aided by future increase in computational resources and technical development in program codes, will become more and more important for more

understanding on the basic electronic properties and the following construction of a large material database and automatic high-throughput materials screening in the near future.

Acknowledgements This work was supported by Grants-in-Aid for Scientific Research (C) (No. 18K03458), on Innovative Areas "3D Active-Site Science" (No. 26105011) and "Hydrogenomics" (No. 18H05519), and for Fund for the Promotion of Joint International Research (Fostering Joint International Research) (No. 16KK0115) from the Japan Society for the Promotion of Science (JSPS), by "Joint Usage/Research Center for Interdisciplinary Large-scale Information Infrastructures" and "High Performance Computing Infrastructure" in Japan (Project ID: jh180069-NAH), and by the Cooperative Research Program of Network Joint Research Center for Materials and Devices in ISIR, Osaka University. We acknowledge the Supercomputer Center, the Institute for Solid State Physics, the University of Tokyo, and the Cyberscience Center, Tohoku University, for the use of their facilities.

References

1. J.R. Sheats, Manufacturing and commercialization issues in organic electronics. J. Mater. Res. **19**(7), 1974 (2004). https://doi.org/10.1557/JMR.2004.0275
2. M.E. Gershenson, V. Podzorov, A.F. Morpurgo, Colloquium: electronic transport in single-crystal organic transistors. Rev. Mod. Phys. **78**, 973 (2006). https://doi.org/10.1103/RevModPhys.78.973
3. J. Kleis, B.I. Lundqvist, D.C. Langreth, E. Schröder, Towards a working density-functional theory for polymers: first-principles determination of the polyethylene crystal structure. Phys. Rev. B **76**, 100201 (2007)
4. D. Lu, Y. Li, D. Rocca, G. Galli, Ab initio calculation of van der waals bonded molecular crystals. Phys. Rev. Lett. **102**, 206411 (2009)
5. A. Tkatchenko, M. Scheffler, Accurate molecular van der waals interactions from ground-state electron density and free-atom reference data. Phys. Rev. Lett. **102**, 073005 (2009)
6. A. Otero-de-la-Roza, E.R. Johnson, Van der waals interactions in solids using the exchange-hole dipole moment model. J. Chem. Phys. **136**, 174109 (2012)
7. A. Otero-de-la-Roza, E.R. Johnson, Application of the exchange-hole dipole moment (XDM) model to molecular solids. J. Chem. Phys. **137**, 054103 (2012)
8. A. Tkatchenko, J.R.A. DiStasio, R. Car, M. Scheffler, Accurate and efficient method for many-body van der waals interactions. Phys. Rev. Lett. **108**, 236402 (2012)
9. J. Klimeš, A. Michaelides, Perspective: advances and challenges in treating van der waals dispersion forces in density functional theory. J. Chem. Phys. **137**, 120901 (2012)
10. I. Hamada, van der waals density functional made accurate. Phys. Rev. B **89**, 121103(R) (2014)
11. A.M. Reilly, A. Tkatchenko, Role of dispersion interactions in the polymorphism and entropic stabilization of the aspirin crystal. Phys. Rev. Lett. **113**, 055701 (2014)
12. L. Hedin, New method for calculating the one-particle green's function with application to the electron-gas problem. Phys. Rev. **139**, A796 (1965). https://doi.org/10.1103/PhysRev.139.A796
13. S. Yanagisawa, I. Hamada, Determination of geometric and electronic structures of organic crystals from first principles: role of the molecular configuration on the electronic structure. J. Appl. Phys. **121**(4), 045501 (2017). https://doi.org/10.1063/1.4974844
14. N. Marzari, A.A. Mostofi, J.R. Yates, I. Souza, D. Vanderbilt, Maximally localized wannier functions: theory and applications. Rev. Mod. Phys. **84**, 1419 (2012)

15. A.A. Mostofi, J.R. Yates, Y.S. Lee, I. Souza, D. Vanderbilt, N. Marzari, wannier90: a tool for obtaining maximally-localised wannier functions. Comput. Phys. Commun. **178**(9), 685 (2008)
16. C. Motta, S. Sanvito, Charge transport properties of durene crystals from first-principles. J. Chem. Theor. Comput. **10**, 4624 (2014)
17. H. Ishii, K. Sugiyama, E. Ito, K. Seki, Energy level alignment and interfacial electronic structures at organic/metal and organic/organic interfaces. Adv. Mater. **11**, 605 (1999)
18. M.S. Hybertsen, S.G. Louie, Electron correlation in semiconductors and insulators: band gaps and quasiparticle energies. Phys. Rev. B **34**, 5390 (1986). https://doi.org/10.1103/PhysRevB.34.5390
19. S.A. Wella, H. Sawada, N. Kawaguchi, F. Muttaqien, K. Inagaki, I. Hamada, Y. Morikawa, Y. Hamamoto, Hybrid image potential states in molecular overlayers on graphene. Phys. Rev. Mater. **1**(6), 061001 (2017). https://doi.org/10.1103/PhysRevMaterials.1.061001
20. T. Yamada, M. Isobe, M. Shibuta, H.S. Kato, T. Munakata, Spectroscopic investigation of unoccupied states in nano- and macroscopic scale: naphthalene overlayers on highly oriented pyrolytic graphite studied by combination of scanning tunneling microscopy and two-photon photoemission. J. Phys. Chem. C **118**(2), 1035 (2014). https://doi.org/10.1021/jp4097875
21. Y. Kang, S.H. Jeon, Y. Cho, S. Han, Ab initio calculation of ionization potential and electron affinity in solid-state organic semiconductors. Phys. Rev. B **93**, 035131 (2016). https://doi.org/10.1103/PhysRevB.93.035131
22. K. Yamada, S. Yanagisawa, T. Koganezawa, K. Mase, N. Sato, H. Yoshida, Impact of the molecular quadrupole moment on ionization energy and electron affinity of organic thin films: experimental determination of electrostatic potential and electronic polarization energies. Phys. Rev. B **97**, 245206 (2018). https://doi.org/10.1103/PhysRevB.97.245206
23. J. Li, G. D'Avino, I. Duchemin, D. Beljonne, X. Blase, Combining the many-body GW formalism with classical polarizable models: insights on the electronic structure of molecular solids. J. Phys. Chem. Lett. **7**(14), 2814 (2016). https://doi.org/10.1021/acs.jpclett.6b01302
24. J.L. Brédas, J.P. Calbert, D.A. da Silva Filho, J. Cornil, Organic semiconductors: a theoretical characterization of the basic parameters governing charge transport. Proc. Natl. Acad. Sci. U. S. A. **99**, 5804 (2002)
25. V. Coropceanu, J. Cornil, D.A. da Silva Filho, Y. Olivier, R. Silbey, J.L. Brédas, Charge transport in organic semiconductors. Chem. Rev. **107**, 926 (2007)
26. A.M. Reilly, R.I. Cooper, C.S. Adjiman, S. Bhattacharya, A.D. Boese, J.G. Brandenburg, P.J. Bygrave, R. Bylsma, J.E. Campbell, R. Car, D.H. Case, R. Chadha, J.C. Cole, K. Cosburn, H.M. Cuppen, F. Curtis, G.M. Day, R.A. DiStasio Jr, A. Dzyabchenko, B.P. van Eijck, D.M. Elking, J.A. van den Ende, J.C. Facelli, M.B. Ferraro, L. Fusti-Molnar, C.A. Gatsiou, T.S. Gee, R. de Gelder, L.M. Ghiringhelli, H. Goto, S. Grimme, R. Guo, D.W.M. Hofmann, J. Hoja, R.K. Hylton, L. Iuzzolino, W. Jankiewicz, D.T. de Jong, J. Kendrick, N.J.J. de Klerk, H.Y. Ko, L.N. Kuleshova, X. Li, S. Lohani, F.J.J. Leusen, A.M. Lund, J. Lv, Y. Ma, N. Marom, A.E. Masunov, P. McCabe, D.P. McMahon, H. Meekes, M.P. Metz, A.J. Misquitta, S. Mohamed, B. Monserrat, R.J. Needs, M.A. Neumann, J. Nyman, S. Obata, H. Oberhofer, A.R. Oganov, A.M. Orendt, G.I. Pagola, C.C. Pantelides, C.J. Pickard, R. Podeszwa, L.S. Price, S.L. Price, A. Pulido, M.G. Read, K. Reuter, E. Schneider, C. Schober, G.P. Shields, P. Singh, I.J. Sugden, K. Szalewicz, C.R. Taylor, A. Tkatchenko, M.E. Tuckerman, F. Vacarro, M. Vasileiadis, A. Vazquez-Mayagoitia, L. Vogt, Y. Wang, R.E. Watson, G.A. de Wijs, J. Yang, Q. Zhu, C.R. Groom, Report on the sixth blind test of organic crystal structure prediction methods. Acta Crystallogr. B **72**(4), 439 (2016). https://doi.org/10.1107/S2052520616007447
27. J. Hermann, R.A. DiStasio, A. Tkatchenko, First-principles models for van der waals interactions in molecules and materials: concepts, theory, and applications. Chem. Rev. **117**(6), 4714 (2017). https://doi.org/10.1021/acs.chemrev.6b00446. PMID: 28272886
28. J. Klimeš, M. Kaltak, E. Maggio, G. Kresse, Singles correlation energy contributions in solids. J. Chem. Phys. **143**(10), 102816 (2015)

29. J. Klimeš, Lattice energies of molecular solids from the random phase approximation with singles corrections. J. Chem. Phys. **145**(9), 094506 (2016). https://doi.org/10.1063/1.4962188. http://scitation.aip.org/content/aip/journal/jcp/145/9/10.1063/1.4962188
30. K. Hongo, M.A. Watson, R.S. Sánchez-Carrera, T. Iitaka, A. Aspuru-Guzik, Failure of conventional density functionals for the prediction of molecular crystal polymorphism: a quantum monte carlo study. J. Phys. Chem. Lett. **1**(12), 1789 (2010)
31. A. Zen, J.G. Brandenburg, J. Klimeš, A. Tkatchenko, D. Alfè, A. Michaelides, Fast and accurate quantum monte carlo for molecular crystals. Proc. Natl. Acad. Sci. U. S. A. **115**(8), 1724 (2018). https://doi.org/10.1073/pnas.1715434115. http://www.pnas.org/content/115/8/1724
32. J. Yang, W. Hu, D. Usvyat, D. Matthews, M. Schütz, G.K.L. Chan, Ab initio determination of the crystalline benzene lattice energy to sub-kilojoule/mole accuracy. Science **345**(6197), 640 (2014)
33. M. Del Ben, J. Hutter, J. VandeVondele, Forces and stress in second order møller-plesset perturbation theory for condensed phase systems within the resolution-of-identity gaussian and plane waves approach. J. Chem. Phys. **143**(10), 102803 (2015)
34. M. Dion, H. Rydberg, E. Schröder, D.C. Langreth, B.I. Lundqvist, Van der waals density functional for general geometries. Phys. Rev. Lett. **92**, 246401 (2004)
35. K. Berland, P. Hyldgaard, Exchange functional that tests the robustness of the plasmon description of the van der waals density functional. Phys. Rev. B **89**, 035412 (2014)
36. J. Kilmeš, D.R. Bowler, A. Michaelides, Chemical accuracy for the van der waals density functional. J. Phys. Condens. Matter **22**, 022201 (2010)
37. K. Lee, É.D. Murray, L. Kong, B.I. Lundqvist, D.C. Langreth, Higher-accuracy van der waals density functional. Phys. Rev. B **82**, 081101(R) (2010)
38. V.R. Cooper, Van der waals density functional: an appropriate exchange functional. Phys. Rev. B **81**, 161104(R) (2010)
39. J. Kilmeš, D.R. Bowler, A. Michaelides, Van derwaals density functionals applied to solids. Phys. Rev. B **83**, 195131 (2011)
40. G. Román-Pérez, J.M. Soler, Efficient implementation of a van der waals density functional: application to double-wall carbon nanotubes. Phys. Rev. Lett. **103**, 096102 (2009). https://doi.org/10.1103/PhysRevLett.103.096102
41. S. Yanagisawa, K. Yamauchi, T. Inaoka, T. Oguchi, I. Hamada, Origin of the band dispersion in a metal phthalocyanine crystal. Phys. Rev. B **90**, 245141 (2014)
42. The crystal structure for the naphthalene at 5 K was taken from NAPHTA31 in Cambridge Crystallographic database. The structure of anthracene was taken from Ref. [68]. The crystal structure of the tetracene crystal was generated using the atomic coordinates given in Ref. [46]. The pentacene crystalline phase obtained by vapor deposition [48] was taken. The diffraction data measured at 123 K [57] was used for hexacene crystal
43. H.C. Alt, J. Kalus, X-ray powder diffraction investigation of naphthalene up to 0.5 gpa. Acta Crystallogr. B Struct. Crystallogr. Cryst. Chem. **38**, 2595 (1982)
44. R. Mason, The crystallography of anthracene at 95 °K and 290 °K. Acta Cryst. **17**, 547 (1964)
45. J.M. Robertson, V.C. Sinclair, J. Trotter, The crystal and molecular structure of tetracene. Acta Cryst. **14**, 697 (1961)
46. The temperature at which the X-ray diffraction measurement is performed is not clear in Ref. [46]. The cell lengths and the volume of the tetracene crystal ($P\bar{1}$ symmetry) measured at 295 K [54] were slightly smaller. Therefore we presume that the temperature of the measurement in Ref. [46] is 295 K or higher
47. T. Siegrist, C. Kloc, J.H. Schön, B. Batlogg, R.C. Haddon, S. Berg, G.A. Thomas, Enhanced physical properties in a pentacene polymorph. Angew. Chem. Int. Ed. Engl. **40**, 1732 (2001)
48. C.C. Mattheus, A.B. Dros, J. Baas, A. Meetsma, J.L. de Boer, T.T.M. Palstra, Polymorphism in pentacene. Acta Crystallogr. C Cryst. Struct. Commun. **C57**, 939 (2001)
49. C.C. Mattheus, A.B. Dros, J. Baas, G.T. Oostergetel, A. Meetsma, J.L. de Boer, T.T.M. Palstra, Identification of polymorphs of pentacene. Synth. Met. **138**, 475 (2003)

50. D. Holmes, S. Kumaraswamy, A. Matzeger, K.P.C. Vollhardt, On the nature of nonplanarity in the [n]phenylenes. Chem.-Eur. J. **5**, 3399 (1999)
51. S. Yanagisawa, K. Okuma, T. Inaoka, I. Hamada, Recent progress in predicting structural and electronic properties of organic solids with the van der waals density functional. J. Electron Spectros. Relat. Phenomena **204**, 159 (2015). https://doi.org/10.1016/j.elspec.2015.04.007. http://www.sciencedirect.com/science/article/pii/S0368204815000754
52. T. Rangel, K. Berland, S. Sharifzadeh, F. Brown-Altvater, K. Lee, P. Hyldgaard, L. Kronik, J.B. Neaton, Structural and excited-state properties of oligoacene crystals from first principles. Phys. Rev. B **93**(11), 115206 (2016)
53. R.B. Campbell, J.M. Robertson, J. Trotter, The crystal structure of hexacene, and a revision of the crystallographic data for tetracene. Acta Cryst. **15**, 289 (1962)
54. H. Yoshida, N. Sato, Grazing-incidence x-ray diffraction study of pentacene thin films with the bulk phase structure. Appl. Phys. Lett. **89**(10), 101919 (2006). https://doi.org/10.1063/1.2349307
55. S. Schiefer, M. Huth, A. Dobrinevski, B. Nickel, Determination of the crystal structure of substrate-induced pentacene polymorphs in fiber structured thin films. J. Am. Chem. Soc. **129**(34), 10316 (2007). https://doi.org/10.1021/ja0730516
56. M. Watanabe, Y.J. Chang, S.W. Liu, T.H. Chao, K. Goto, M.M. Islam, C.H. Yuan, Y.T. Tao, T. Shinmyozu, T.J. Chow, The synthesis, crystal structure and charge-transport properties of hexacene. Nat. Chem. **4**, 574 (2012). https://doi.org/10.1038/nchem.1381
57. P.E. Blöchl, Projector augmented-wave method. Phys. Rev. B **50**, 17953 (1994)
58. G. Kresse, J. Furthmüller, Efficiency of ab-initio total energy calculations for metals and semiconductors using a plane-wave basis set. Comput. Mater. Sci. **6**, 15 (1996)
59. G. Kresse, D. Joubert, From ultrasoft pseudopotentials to the projector augmented-wave method. Phys. Rev. B **59**, 1758 (1999)
60. A.D. Becke, On the large-gradient behavior of the density functional exchange energy. J. Chem. Phys. **85**, 7184 (1986)
61. We used `C_h` and `H_h` for our vdW-DF calculations
62. H.J. Monkhorst, J.D. Pack, Special points for Brillouin-zone integrations. Phys. Rev. B **13**, 5188 (1976). https://doi.org/10.1103/PhysRevB.13.5188
63. F. Murnaghan, The compressibility of media under extreme pressures. Proc. Natl. Acad. Sci. U. S. A. **30**(9), 244 (1944)
64. A.M. Reilly, A. Tkatchenko, Understanding the role of vibrations, exact exchange, and many-body van der waals interactions in the cohesive properties of molecular crystals. J. Chem. Phys. **139**, 024705 (2013)
65. D.J. Carter, A.L. Rohl, Benchmarking calculated lattice parameters and energies of molecular crystals using van der waals density functionals. J. Chem. Theory Comput. **10**(8), 3423 (2014)
66. S.C. Capelli, A. Albinati, S.A. Mason, B.T.M. Willis, Molecular motion in crystalline naphthalene: analysis of multi-temperature x-ray and neutron diffraction data. J. Phys. Chem. A **110**(41), 11695 (2006). https://doi.org/10.1021/jp062953a
67. S.L. Chaplot, N. Lehner, G.S. Pawley, The structure of anthracene-$d_1 0$ at 16 K using neutron diffraction. Acta Crystallogr. B **38**(2), 483 (1982). https://doi.org/10.1107/S0567740882003239
68. M.V. Roux, M. Temprado, J.S. Chickos, Y. Nagano, Critically evaluated thermochemical properties of polycyclic aromatic hydrocarbons. J. Phys. Chem. Ref. Data **37**(4), 1855 (2008). https://doi.org/10.1063/1.2955570
69. A.D. Becke, E.R. Johnson, Exchange-hole dipole moment and the dispersion interaction revisited. J. Chem. Phys. **127**, 154108 (2007)
70. A.D. Becke, E.R. Johnson, A unified density-functional treatment of dynamical, nondynamical, and dispersion correlations. J. Chem. Phys. **127**, 124108 (2007)
71. N. Geacintov, M. Pope, Low-lying valence band states and intrinsic photoconductivity in crystalline anthracene and tetracene. J. Chem. Phys. **50**(2), 814 (1969)
72. C.L. Braun, G.M. Dobbs, Intrinsic photoconductivity in naphthalene single crystals. J. Chem. Phys. **53**(7), 2718 (1970)

73. H. Baessler, H. Killesreiter, Hot carrier injection into molecular crystals and its relevance to the field dependence of photocurrents. Phys. Status Solidi B **53**(1), 183 (1972)
74. H. Baessler, H. Killesreiter, Bandgap-determination from autoionization data in molecular crystals. Mol. Cryst. Liq. Cryst. **24**(1–2), 21 (1973)
75. A.I. Belkind, V.V. Grechov, Energy levels of polyacene crystals. Phys. Status Solidi A **26**(1), 377 (1974)
76. L. Sebastian, G. Weiser, H. Bässler, Charge transfer transitions in solid tetracene and pentacene studied by electroabsorption. Chem. Phys. **61**, 125 (1981)
77. E.A. Silinsh, V.A. Kolesnikov, I.J. Muzikante, D.R. Balode, On charge carrier photogeneration mechanisms in organic molecular crystals. Phys. Status Solidi B **113**(1), 379 (1982)
78. L. Sebastian, G. Weiser, G. Peter, H. Bässler, Charge-transfer transitions in crystalline anthracene and their role in photoconductivity. Chem. Phys. **75**, 103 (1983)
79. Y. Isono, E. Morikawa, M. Kotani, Two-color pulsed photoconductivity study of naphthalene single crystal: photoionization of singlet exciton. Chem. Phys. Lett. **125**, 344 (1986)
80. H. Yoshida, K. Yamada, J. Tsutsumi, N. Sato, Complete description of ionization energy and electron affinity in organic solids: determining contributions from electronic polarization, energy band dispersion, and molecular orientation. Phys. Rev. B **92**, 075145 (2015). https://doi.org/10.1103/PhysRevB.92.075145
81. M.L.M. Rocco, M. Haeming, D.R. Batchelor, R. Fink, A. Schöll, E. Umbach, Electronic relaxation effects in condensed polyacenes: a high-resolution photoemission study. J. Chem. Phys. **129**(7), 074702 (2008). https://doi.org/10.1063/1.2966356
82. M.M. Rieger, L. Steinbeck, I.D. White, H.N. Rojas, R.W. Godby, The GW space-time method for the self-energy of large systems. Comput. Phys. Commun. **117**, 211 (1999)
83. L. Steinbeck, A. Rubio, L. Reining, M. Torrent, I.D. White, R.W. Godby, Enhancements to the GW space-time method. Comput. Phys. Commun. **125**, 105 (2000)
84. C. Freysoldt, P. Eggert, P. Rinke, A. Schindlmayr, R.W. Godby, M. Scheffler, Dielectric anisotropy in the GW space-time method. Comput. Phys. Commun. **176**, 1 (2007)
85. N. Troullier, J.L. Martins, Efficient pseudopotentials for place-wave calculations. Phys. Rev. B **43**, 1993 (1991)
86. J.P. Perdew, K. Burke, M. Ernzerhof, Generalized gradient approximation made simple. Phys. Rev. Lett. **77**(18), 3865 (1996)
87. Y. Morikawa, H. Ishii, K. Seki, Theoretical study of n-alkane adsorption on metal surfaces. Phys. Rev. B **69**, 041403(R) (2004)
88. C. Faber, P. Boulanger, C. Attaccalite, I. Duchemin, X. Blase, Excited states properties of organic molecules: from density functional theory to the GW and bethe–salpeter green's function formalisms. Phil. Trans. R. Soc. A **372**(2011) (2014)
89. S. Körbel, P. Boulanger, I. Duchemin, X. Blase, M.A.L. Marques, S. Botti, Benchmark many-body GW and bethe-salpeter calculations for small transition metal molecules. J. Chem. Theory Comput. **10**(9), 3934 (2014)
90. C. Rostgaard, K.W. Jacobsen, K.S. Thygesen, Fully self-consistent GW calculations for molecules. Phys. Rev. B **81**, 085103 (2010)
91. X. Blase, C. Attaccalite, V. Olevano, First-principles *GW* calculations for fullerenes, porphyrins, phtalocyanine, and other molecules of interest for organic photovoltaic applications. Phys. Rev. B **83**, 115103 (2011)
92. S. Sharifzadeh, A. Biller, L. Kronik, J.B. Neaton, Quasiparticle and optical spectroscopy of the organic semiconductors pentacene and ptcda from first principles. Phys. Rev. B **85**, 125307 (2012)
93. F. Caruso, P. Rinke, X. Ren, M. Scheffler, A. Rubio, Unified description of ground and excited states of finite systems: the self-consistent *GW* approach. Phys. Rev. B **86**, 081102 (2012)
94. F. Bruneval, M.A.L. Marques, Benchmarking the starting points of the GW approximation for molecules. J. Chem. Theory Comput. **9**(1), 324 (2013)
95. M. Govoni, G. Galli, Large scale GW calculations. J. Chem. Theory Comput. **11**(6), 2680 (2015)

96. W. Luo, S. Ismail-Beigi, M.L. Cohen, S.G. Louie, Quasiparticle band structure of zns and znse. Phys. Rev. B **66**, 195215 (2002)
97. W. Setyawan, S. Curtarolo, High-throughput electronic band structure calculations: challenges and tools. Comput. Mater. Sci. **49**, 299 (2010)
98. S. Yanagisawa, Y. Morikawa, A. Schindlmayr, Homo band dispersion of crystalline rubrene: effects of self-energy corrections within the *GW* approximation. Phys. Rev. B **88**, 115438 (2013)
99. S. Yanagisawa, Y. Morikawa, A. Schindlmayr, Theoretical investigation of the band structure of picene single crystals within the *GW* approximation. Jpn. J. Appl. Phys. **53**, 05FY02 (2014)
100. E.L. Shirley, Many-body effects on bandwidths in ionic, noble gas, and molecular solids. Phys. Rev. B **58**, 9579 (1998)
101. E. Kwon, H. Oikawa, H. Kasai, H. Nakanishi, A fabrication method of organic nanocrystals using stabilizer-free emulsion. Cryst. Growth Des. **7**(4), 600 (2007)
102. N. Ueno, S. Kera, Electron spectroscopy of functional organic thin films: deep insights into valence electronic structure in relation to charge transport property. Prog. Surf. Sci. **83**(10–12), 490 (2008)
103. S. Ciuchi, R.C. Hatch, H. Höchst, C. Faber, X. Blase, S. Fratini, Molecular fingerprints in the electronic properties of crystalline organic semiconductors: from experiments to theory. Phys. Rev. Lett. **108**, 256401 (2012)
104. K.H. Frank, P. Yannoulis, R. Dudde, E.E. Koch, Unoccupied molecular orbitals of aromatic hydrocarbons adsorbed on ag(111). J. Chem. Phys. **89**(12), 7569 (1988). https://doi.org/10.1063/1.455720
105. Y. Li, V. Coropceanu, J.L. Brédas, Thermal narrowing of the electronic bandwidths in organic molecular semiconductors: impact of the crystal thermal expansion. J. Phys. Chem. Lett. **3**(22), 3325 (2012). https://doi.org/10.1021/jz301575u
106. Y.C. Cheng, R.J. Silbey, D.A. da Silva Filho, J.P. Calbert, J. Cornil, J.L. Brédas, Three-dimensional band structure and bandlike mobility in oligoacene single crystals: a theoretical investigation. J. Chem. Phys. **118**(8), 3764 (2003)
107. G.A. de Wijs, C.C. Mattheus, R.A. de Groot, T.T. Palstra, Anisotropy of the mobility of pentacene from frustration. Synth. Met. **139**(1), 109 (2003)
108. H. Yoshida, N. Sato, Crystallographic and electronic structures of three different polymorphs of pentacene. Phys. Rev. B **77**, 235205 (2008)
109. D.A. da Silva Filho, E.G. Kim, J.L. Brédas, Transport properties in the rubrene crystal: electronic coupling and vibrational reorganization energy. Adv. Mater. **17**, 1072 (2005)
110. S.Y. Quek, M. Kamenetska, M.L. Steigerwald, H.J. Choi, S.G. Louie, M.S. Hybertsen, J.B. Neaton, L. Venkataraman, Mechanically controlled binary conductance switching of a single-molecule junction. Nat. Nanotechnol. **4**, 230 EP (2009). https://doi.org/10.1038/nnano.2009.10
111. J.C. Inkson, Many-body effect at metal-semiconductor junctions. II. The self energy and band structure distortion. J. Phys. C Solid State Phys. **6**(8), 1350 (1973). http://stacks.iop.org/0022-3719/6/i=8/a=004
112. J.B. Neaton, M.S. Hybertsen, S.G. Louie, Renormalization of molecular electronic levels at metal-molecule interfaces. Phys. Rev. Lett. **97**, 216405 (2006). https://doi.org/10.1103/PhysRevLett.97.216405
113. J.M. Garcia-Lastra, C. Rostgaard, A. Rubio, K.S. Thygesen, Polarization-induced renormalization of molecular levels at metallic and semiconducting surfaces. Phys. Rev. B **80**(24), 245427 (2009). https://doi.org/10.1103/PhysRevB.80.245427
114. Y. Chen, I. Tamblyn, S.Y. Quek, Energy level alignment at hybridized organic–metal interfaces: the role of many-electron effects. J. Phys. Chem. C **121**(24), 13125 (2017). https://doi.org/10.1021/acs.jpcc.7b00715
115. I. Tamblyn, P. Darancet, S.Y. Quek, S.A. Bonev, J.B. Neaton, Electronic energy level alignment at metal-molecule interfaces with a *GW* approach. Phys. Rev. B **84**(20), 201402 (2011). https://doi.org/10.1103/PhysRevB.84.201402

116. S.Y. Quek, L. Venkataraman, H.J. Choi, S.G. Louie, M.S. Hybertsen, J.B. Neaton, Amine-gold linked single-molecule circuits: experiment and theory. Nano Lett. **7**(11), 3477 (2007). https://doi.org/10.1021/nl072058i
117. D.A. Egger, Z.F. Liu, J.B. Neaton, L. Kronik, Reliable energy level alignment at physisorbed molecule–metal interfaces from density functional theory. Nano Lett. **15**(4), 2448 (2015). https://doi.org/10.1021/nl504863r
118. L. Kronik, T. Stein, S. Refaely-Abramson, R. Baer, Excitation gaps of finite-sized systems from optimally tuned range-separated hybrid functionals. J. Chem. Theory Comput. **8**(5), 1515 (2012). https://doi.org/10.1021/ct2009363
119. R. Baer, E. Livshits, U. Salzner, Tuned range-separated hybrids in density functional theory. Annu. Rev. Phys. Chem. **61**(1), 85 (2010). https://doi.org/10.1146/annurev.physchem.012809.103321
120. Z.F. Liu, D.A. Egger, S. Refaely-Abramson, L. Kronik, J.B. Neaton, Energy level alignment at molecule-metal interfaces from an optimally tuned range-separated hybrid functional. J. Chem. Phys. **146**(9), 092326 (2017). https://doi.org/10.1063/1.4975321
121. P.M. Echenique, J.B. Pendry, The existence and detection of Rydberg states at surfaces. J. Phys. C Solid State Phys. **11**(10), 2065 (1978). http://stacks.iop.org/0022-3719/11/i=10/a=017
122. P.M. Echenique, J.B. Pendry, Theory of image states at metal surfaces. Prog. Surf. Sci. **32**(2), 111 (1989). https://doi.org/10.1016/0079-6816(89)90015-4. http://www.sciencedirect.com/science/article/pii/0079681689900154
123. I.R. Collins, P.T. Andrews, A.R. Law, Unoccupied electronic states of single-crystal graphite by angle-resolved ultraviolet inverse photoemission. Phys. Rev. B **38**, 13348 (1988). https://doi.org/10.1103/PhysRevB.38.13348
124. J. Lehmann, M. Merschdorf, A. Thon, S. Voll, W. Pfeiffer, Properties and dynamics of the image potential states on graphite investigated by multiphoton photoemission spectroscopy. Phys. Rev. B **60**(24), 17037 (1999). https://doi.org/10.1103/PhysRevB.60.17037
125. M. Zamkov, N. Woody, S. Bing, H.S. Chakraborty, Z. Chang, U. Thumm, P. Richard, Time-resolved photoimaging of image-potential states in carbon nanotubes. Phys. Rev. Lett. **93**, 156803 (2004). https://doi.org/10.1103/PhysRevLett.93.156803
126. M. Feng, J. Zhao, H. Petek, Atomlike, hollow-core–bound molecular orbitals of c60. Science **320**(5874), 359 (2008). https://doi.org/10.1126/science.1155866. http://science.sciencemag.org/content/320/5874/359
127. J. Zhao, M. Feng, J. Yang, H. Petek, The superatom states of fullerenes and their hybridization into the nearly free electron bands of fullerites. ACS Nano **3**(4), 853 (2009). https://doi.org/10.1021/nn800834k
128. V.M. Silkin, J. Zhao, F. Guinea, E.V. Chulkov, P.M. Echenique, H. Petek, Image potential states in graphene. Phys. Rev. B **80**(12), 121408 (2009). https://doi.org/10.1103/PhysRevB.80.121408
129. M. Posternak, A. Baldereschi, A.J. Freeman, E. Wimmer, Prediction of electronic surface states in layered materials: graphite. Phys. Rev. Lett. **52**, 863 (1984). https://doi.org/10.1103/PhysRevLett.52.863
130. N.A.W. Holzwarth, S.G. Louie, S. Rabii, X-ray form factors and the electronic structure of graphite. Phys. Rev. B **26**, 5382 (1982). https://doi.org/10.1103/PhysRevB.26.5382
131. T. Fauster, F.J. Himpsel, J.E. Fischer, E.W. Plummer, Three-dimensional energy band in graphite and lithium-intercalated graphite. Phys. Rev. Lett. **51**, 430 (1983). https://doi.org/10.1103/PhysRevLett.51.430
132. S. Bose, V.M. Silkin, R. Ohmann, I. Brihuega, L. Vitali, C.H. Michaelis, P. Mallet, J.Y. Veuillen, M.A. Schneider, E.V. Chulkov, P.M. Echenique, K. Kern, Image potential states as a quantum probe of graphene interfaces. New J. Phys. **12**(2), 023028 (2010)
133. I.D. White, R.W. Godby, M.M. Rieger, R.J. Needs, Dynamic image potential at an al(111) surface. Phys. Rev. Lett. **80**, 4265 (1998). https://doi.org/10.1103/PhysRevLett.80.4265
134. I. Hamada, Y. Hamamoto, Y. Morikawa, Image potential states from the van der waals density functional. J. Chem. Phys. **147**(4), 044708 (2017). https://doi.org/10.1063/1.4995441

135. O. Leenaerts, B. Partoens, F.M. Peeters, A. Volodin, C.V. Haesendonck, The work function of few-layer graphene. J. Phys. Condens. Matter **29**(3), 035003 (2017). http://stacks.iop.org/0953-8984/29/i=3/a=035003
136. I. Hamada, S. Yanagisawa, Pseudopotential approximation in van der waals density functional calculations. Phys. Rev. B **84**, 153104 (2011). https://doi.org/10.1103/PhysRevB.84.153104
137. N. Ferri, A. Ambrosetti, A. Tkatchenko, Electronic charge rearrangement at metal/organic interfaces induced by weak van der waals interactions. Phys. Rev. Mater. **1**, 026003 (2017). https://doi.org/10.1103/PhysRevMaterials.1.026003
138. N. Ferri, R.A. DiStasio, A. Ambrosetti, R. Car, A. Tkatchenko, Electronic properties of molecules and surfaces with a self-consistent interatomic van der waals density functional. Phys. Rev. Lett. **114**, 176802 (2015). https://doi.org/10.1103/PhysRevLett.114.176802
139. M. Shibuta, N. Hirata, T. Eguchi, A. Nakajima, Probing of an adsorbate-specific excited state on an organic insulating surface by two-photon photoemission spectroscopy. J. Am. Chem. Soc. **136**(5), 1825 (2014)
140. M. Shibuta, N. Hirata, R. Matsui, M. Nakaya, T. Eguchi, A. Nakajima, Excitation and relaxation dynamics of two-dimensional photoexcited electrons on alkanethiolate self-assembled monolayers. J. Phys. Chem. C **119**(40), 22945 (2015)
141. M. Shibuta, N. Hirata, T. Eguchi, A. Nakajima, Photoexcited state confinement in two-dimensional crystalline anthracene monolayer at room temperature. ACS Nano **11**(4), 4307 (2017)
142. T. Yamada, M. Shibuta, Y. Ami, Y. Takano, A. Nonaka, K. Miyakubo, T. Munakata, Novel growth of naphthalene overlayer on Cu(111) studied by STM, LEED, and 2PPE. J. Phys. Chem. C **114**(31), 13334 (2010)
143. C. Bondi, P. Baglioni, G. Taddei, Structure of the monolayers of aromatic molecules adsorbed on graphite. Chem. Phys. **96**(2), 277 (1985). https://doi.org/10.1016/0301-0104(85)85091-6. http://www.sciencedirect.com/science/article/pii/0301010485850916
144. U. Bardi, S. Magnanelli, G. Rovida, Leed study of benzene and naphthalene monolayers adsorbed on the basal plane of graphite. Langmuir **3**(2), 159 (1987). https://doi.org/10.1021/la00074a003
145. T. Yamada, Y. Takano, M. Isobe, K. Miyakubo, T. Munakata, Growth and adsorption geometry of naphthalene overlayers on HOPG studied by low-temperature scanning tunneling microscopy. Chem. Phys. Lett. **546**, 136 (2012). https://doi.org/10.1016/j.cplett.2012.08.011. http://www.sciencedirect.com/science/article/pii/S0009261412009128
146. F. Sojka, M. Meissner, T. Yamada, T. Munakata, R. Forker, T. Fritz, Naphthalene's six shades on graphite: a detailed study on the polymorphism of an apparently simple system. J. Phys. Chem. C **120**(40), 22972 (2016). https://doi.org/10.1021/acs.jpcc.6b06702
147. S. Okada, Y. Enomoto, K. Shiraishi, A. Oshiyama, New electron states that float on semiconductor and metal surfaces. Surf. Sci. **585**(3), L177 (2005)
148. M. Kutschera, M. Weinelt, M. Rohlfing, T. Fauster, Image-potential-induced surface state at si (100). Appl. Phys. A **88**(3), 519 (2007)
149. M. Rohlfing, N.P. Wang, P. Krüger, J. Pollmann, Image states and excitons at insulator surfaces with negative electron affinity. Phys. Rev. Lett. **91**(25), 256802 (2003)
150. B. Baumeier, P. Krüger, J. Pollmann, Bulk and surface electronic structures of alkaline-earth metal oxides: bound surface and image-potential states from first principles. Phys. Rev. B **76**(20), 205404 (2007)
151. S. Saito, A. Oshiyama, Cohesive mechanism and energy bands of solid c_{60}. Phys. Rev. Lett. **66**, 2637 (1991). https://doi.org/10.1103/PhysRevLett.66.2637
152. S. Okada, A. Oshiyama, S. Saito, Nearly free electron states in carbon nanotube bundles. Phys. Rev. B **62**, 7634 (2000). https://doi.org/10.1103/PhysRevB.62.7634
153. S. Okada, S. Saito, A. Oshiyama, Energetics and electronic structures of encapsulated C_{60} in a carbon nanotube. Phys. Rev. Lett. **86**, 3835 (2001). https://doi.org/10.1103/PhysRevLett.86.3835
154. T. Miyake, S. Saito, Electronic structure of potassium-doped carbon nanotubes. Phys. Rev. B **65**, 165419 (2002). https://doi.org/10.1103/PhysRevB.65.165419

155. T. Miyake, S. Saito, Quasiparticle band structure of carbon nanotubes. Phys. Rev. B **68**(15), 155424 (2003)
156. E.R. Margine, V.H. Crespi, Universal behavior of nearly free electron states in carbon nanotubes. Phys. Rev. Lett. **96**, 196803 (2006). https://doi.org/10.1103/PhysRevLett.96.196803
157. S. Hu, J. Zhao, Y. Jin, J. Yang, H. Petek, J. Hou, Nearly free electron superatom states of carbon and boron nitride nanotubes. Nano Lett. **10**(12), 4830 (2010)
158. N. Sato, K. Seki, H. Inokuchi, Polarization energies of organic solids determined by ultraviolet photoelectron spectroscopy. J. Chem. Soc. Faraday Trans. **2**, 1621 (1981)
159. S. Refaely-Abramson, S. Sharifzadeh, M. Jain, R. Baer, J.B. Neaton, L. Kronik, Gap renormalization of molecular crystals from density-functional theory. Phys. Rev. B **88**, 081204 (2013). https://doi.org/10.1103/PhysRevB.88.081204
160. J.E. Norton, J.L. Brédas, Polarization energies in oligoacene semiconductor crystals. J. Am. Chem. Soc. **130**(37), 12377 (2008). https://doi.org/10.1021/ja8017797. PMID: 18715006
161. P.K. Nayak, N. Periasamy, Calculation of electron affinity, ionization potential, transport gap, optical band gap and exciton binding energy of organic solids using 'solvation' model and DFT. Org. Electron. **10**(7), 1396 (2009). https://doi.org/10.1016/j.orgel.2009.06.011. http://www.sciencedirect.com/science/article/pii/S1566119909001815
162. N. Sato, H. Inokuchi, E.A. Silinsh, Reevaluation of electronic polarization energies in organic molecular crystals. Chem. Phys. **115**(2), 269 (1987). https://doi.org/10.1016/0301-0104(87)80041-1. http://www.sciencedirect.com/science/article/pii/0301010487800411
163. W. Kohn, Density functional and density matrix method scaling linearly with the number of atoms. Phys. Rev. Lett. **76**, 3168 (1996). https://doi.org/10.1103/PhysRevLett.76.3168
164. D. Deutsch, A. Natan, Y. Shapira, L. Kronik, Electrostatic properties of adsorbed polar molecules: opposite behavior of a single molecule and a molecular monolayer. J. Am. Chem. Soc. **129**(10), 2989 (2007)
165. B.J. Topham, Z.G. Soos, Ionization in organic thin films: electrostatic potential, electronic polarization, and dopants in pentacene films. Phys. Rev. B **84**, 165405 (2011). https://doi.org/10.1103/PhysRevB.84.165405
166. E.V. Tsiper, Z.G. Soos, Charge redistribution and polarization energy of organic molecular crystals. Phys. Rev. B **64**, 195124 (2001). https://doi.org/10.1103/PhysRevB.64.195124
167. J. Li, G. D'Avino, I. Duchemin, D. Beljonne, X. Blase, Accurate description of charged excitations in molecular solids from embedded many-body perturbation theory. Phys. Rev. B **97**, 035108 (2018). https://doi.org/10.1103/PhysRevB.97.035108
168. W.G. Aulbur, L. Jönsson, J.W. Wilkins, in *Quasiparticle Calculations in Solids*, ed. by H. Ehrenreich, F. Spaepen. Solid State Physics, vol. 54 (Academic, 2000), pp. 1–218. https://doi.org/10.1016/S0081-1947(08)60248-9. http://www.sciencedirect.com/science/article/pii/S0081194708602489
169. I.D. White, R.W. Godby, M.M. Rieger, R.J. Needs, Dynamic image potential at an al(111) surface. Phys. Rev. Lett. **80**(19), 4265 (1998). https://doi.org/10.1103/PhysRevLett.80.4265
170. H. Yoshida, Near-ultraviolet inverse photoemission spectroscopy using ultra-low energy electrons. Chem. Phys. Lett. **539–540**, 180 (2012). https://doi.org/10.1016/j.cplett.2012.04.058. http://www.sciencedirect.com/science/article/pii/S000926141200557X
171. H. Yoshida, Measuring the electron affinity of organic solids: an indispensable new tool for organic electronics. Anal. Bioanal. Chem. **406**(9), 2231 (2014). https://doi.org/10.1007/s00216-014-7659-1
172. H. Yoshida, Principle and application of low energy inverse photoemission spectroscopy: a new method for measuring unoccupied states of organic semiconductors. J. Electron Spectros. Relat. Phenomena **204**, 116 (2015). https://doi.org/10.1016/j.elspec.2015.07.003. http://www.sciencedirect.com/science/article/pii/S0368204815001486